Schildgen, T., Robinson, R. A. J., Savi, S., Phillips, W. M., Spencer, J. Q. G., Bookhagen, B., Scherler, D., Tofelde, S., Alonso, R. N., Kubik, P. W., Binnie, S. A., Strecker, M. R. (2016): Landscape response to late Pleistocene climate change in NW Argentina: Sediment flux modulated by basin geometry and connectivity. - *Journal of Geophysical Research*, *121*, 2, pp. 392—414.

DOI: http://doi.org/10.1002/2015JF003607

AGU PUBLICATIONS

JGR

Journal of Geophysical Research: Earth Surface

RESEARCH ARTICLE

10.1002/2015JF003607

Key Points:
- Antiphased timing of aggradation on west and east sides of valley
- Cosmogenic ^{10}Be erosion rates indicate more landslides when precipitation increases
- Catchment geometry and connectivity dictate location and timing of aggradation

Supporting Information:
- Text S1, Figures S1–S3, and Table S1–S3 Titles
- Figure S1
- Figure S2
- Figure S3

Correspondence to:
T. F. Schildgen,
tschild@gfz-potsdam.de

Citation:
Schildgen, T. F., et al. (2016), Landscape response to late Pleistocene climate change in NW Argentina: Sediment flux modulated by basin geometry and connectivity, *J. Geophys. Res. Earth Surf.*, *121*, 392–414, doi:10.1002/2015JF003607.

Received 7 MAY 2015
Accepted 15 JAN 2016
Accepted article online 28 JAN 2016
Published online 23 FEB 2016

Landscape response to late Pleistocene climate change in NW Argentina: Sediment flux modulated by basin geometry and connectivity

Taylor F. Schildgen[1,2], Ruth A. J. Robinson[3], Sara Savi[1], William M. Phillips[4], Joel Q. G. Spencer[5], Bodo Bookhagen[1], Dirk Scherler[2,6], Stefanie Tofelde[1], Ricardo N. Alonso[7], Peter W. Kubik[8], Steven A. Binnie[9], and Manfred R. Strecker[1]

[1]Institut für Erd- und Umweltwissenschaften, University of Potsdam, Potsdam, Germany, [2]Helmholtz Zentrum Potsdam, Deutsches GeoForschungsZentrum, Potsdam, Germany, [3]Department of Earth and Environmental Sciences, University of St Andrews, St Andrews, UK, [4]Idaho Geological Survey, University of Idaho, Moscow, Idaho, USA, [5]Department of Geology, Kansas State University, Manhattan, Kansas, USA, [6]Institute of Geological Sciences, Freie Universität Berlin, Berlin, Germany, [7]Facultad de Ciencias Naturales-Geología, Universidad Nacional de Salta, Salta, Argentina, [8]Paul Scherrer Institut, c/o Institute of Particle Physics, ETH, Zurich, Switzerland, [9]Department of Geology and Mineralogy, University of Cologne, Cologne, Germany

Abstract Fluvial fill terraces preserve sedimentary archives of landscape responses to climate change, typically over millennial timescales. In the Humahuaca Basin of NW Argentina (Eastern Cordillera, southern Central Andes), our 29 new optically stimulated luminescence ages of late Pleistocene fill terrace sediments demonstrate that the timing of past river aggradation occurred over different intervals on the western and eastern sides of the valley, despite their similar bedrock lithology, mean slopes, and precipitation. In the west, aggradation coincided with periods of increasing precipitation, while in the east, aggradation coincided with decreasing precipitation or more variable conditions. Erosion rates and grain size dependencies in our cosmogenic ^{10}Be analyses of modern and fill terrace sediments reveal an increased importance of landsliding compared to today on the west side during aggradation, but of similar importance during aggradation on the east side. Differences in the timing of aggradation and the ^{10}Be data likely result from differences in valley geometry, which causes sediment to be temporarily stored in perched basins on the east side. It appears as if periods of increasing precipitation triggered landslides throughout the region, which induced aggradation in the west, but blockage of the narrow bedrock gorges downstream from the perched basins in the east. As such, basin geometry and fluvial connectivity appear to strongly influence the timing of sediment movement through the system. For larger basins that integrate subbasins with differing geometries or degrees of connectivity (like Humahuaca), sedimentary responses to climate forcing are likely attenuated.

1. Introduction

Understanding landscape response to climate change is among the key problems in the geosciences today, particularly as global warming is expected to influence not only temperature patterns worldwide but also precipitation patterns and intensity [*Trenberth*, 2011] and flood magnitudes [*Knox*, 1993]. Although general theories regarding orogen-scale responses to climate forcing over millions of years have existed for decades [e.g., *Koons*, 1990; *Beaumont et al*., 1992; *Willett*, 1999; *Hoth et al*., 2006; *Whipple and Meade*, 2006], promising field demonstrations have been limited to where secondary effects like base-level fall have triggered an orogen-scale response [e.g., *Ballato et al*., 2015]. Landscape responses to millennial-scale climate shifts may be even more complex, as local factors including soil properties, vegetation cover, lithology, storm frequency, and landscape history all influence short-term fluctuations in erosion and sediment transport [*Blum and Törnqvist*, 2000; *Bull*, 1991; *Tucker and Slingerland*, 1997; *Istanbulluoglu and Bras*, 2006; *Acosta et al*., 2015; *Scherler et al*., 2015]. One empirical approach to better understanding responses to higher-frequency climate shifts is to reconstruct past changes in erosion rates and processes from sediments within fluvial fill terraces, particularly as terrace formation is often associated with millennial-scale climate shifts [*Bull*, 1991]. The Central Andes are a promising location for such studies, with thick fill terraces preserved along the steep flanks of the Andean Plateau and within the intermontane basins of the Eastern Cordillera [*Robinson et al*., 2005; *Sancho et al*., 2008; *Spencer and Robinson*, 2008; *Pingel et al*., 2013] (Figure 1a), and precipitation regimes that can change suddenly as a result of small shifts in the sharp precipitation gradients [*Bookhagen and Strecker*, 2008] (Figure 1b).

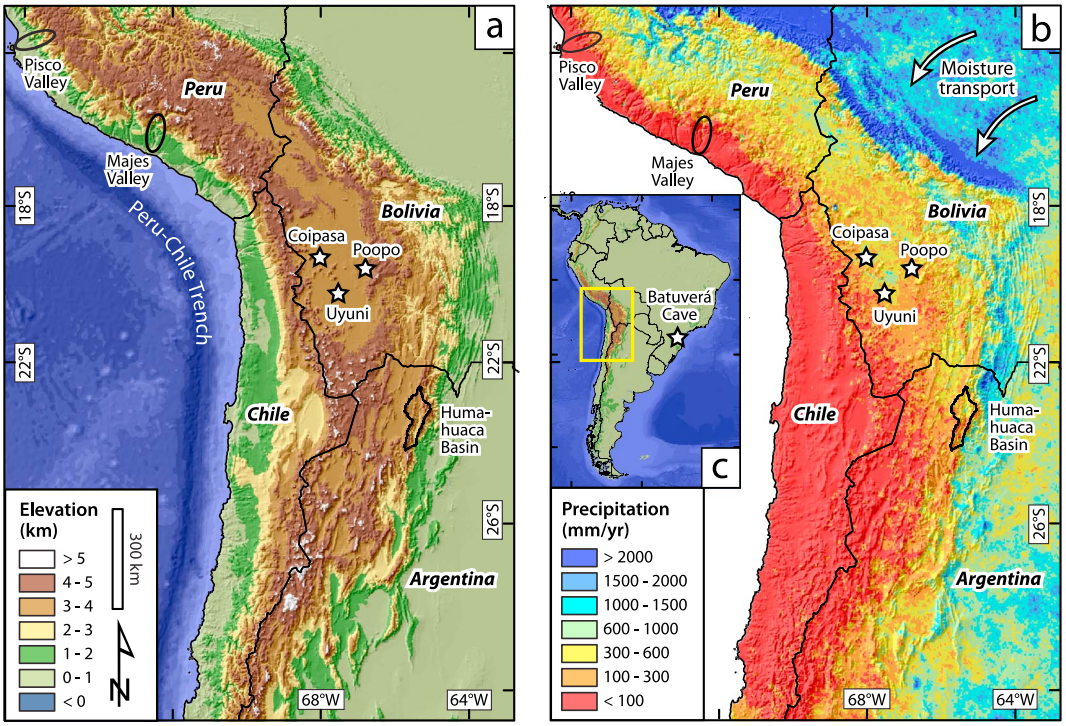

Figure 1. Topography and precipitation of the Central Andes. (a) Topography and bathymetry from ETOPO1 data set. Stars mark locations of paleolake record sites: salars de Coipasa, Poopo, and Uyuni. Ellipses mark locations of western Central Andes fill terrace studies (Pisco and Majes valleys). Catchment of the Humahuaca Basin is outlined in black. (b) Precipitation from TRMM2B31 [*Bookhagen and Strecker*, 2008]. (c) Map of South America. Yellow box shows boundaries of Figures 1a and 1b.

In the western Central Andes, fill terrace formation has been commonly linked to wetter climate periods during the late Quaternary [e.g., *Fontugne et al.*, 1999; *Keefer et al.*, 2003; *Magilligan and Goldstein*, 2001; *Nester et al.*, 2007; *Magilligan et al.*, 2008; *Steffen et al.*, 2009, 2010; *Bekaddour et al.*, 2014]. In both the western and eastern Central Andes, fluvial aggradation has been explained as a result of increased hillslope erosion related to mass movements [*Tchilinguirian and Pereyra*, 2001; *Steffen et al.*, 2009, 2010; *Bekaddour et al.*, 2014] or an increase in periglacial weathering [*May and Soler*, 2010]. A recent study that links a series of large landslides in southern Peru to the "Ouki" wet climatic interval of ~120 to 100 ka [*Margirier et al.*, 2015] supports the importance of sudden mass movements. However, *McPhillips et al.* [2014] interpreted cosmogenic nuclide data from southern Peru to indicate no increased frequency of landslides during a past wet period, and instead suggested that landslides were primarily driven by seismic activity, which has not changed with time above the active subduction zone.

In the eastern Central Andes, a number of large landslide deposits in the NW Argentine Andes were correlated with past wetter climate periods [*Trauth et al.*, 2000, 2003]. Later work raised the possibility that mixing with Tertiary marls may have compromised the ^{14}C ages for those landslides, but ^{10}Be exposure dates confirmed that the landslides indeed cluster during wetter periods [*Hermanns et al.*, 2004]. Only a few large landslides in NW Argentina have been associated with tectonic forcing [*Hermanns and Strecker*, 1999; *Wayne*, 1999], but those are currently undated. Dated fill terraces in the region are limited to the Humahuaca Basin (Figure 1), where the timing of aggradation based on seven OSL dates and two ^{14}C dates spans both wetter and drier climate phases [*Robinson et al.*, 2005; *Sancho et al.*, 2008; *Spencer and Robinson*, 2008; *Pingel et al.*, 2013]. One possible explanation for the lack of a consistent climate-related signal is that the subcatchments have different responses following a change in climate, such as may arise if they have differing thresholds for fluvial incision [*Molnar*, 2001; *Lague et al.*, 2005; *Molnar et al.*, 2006; *DiBiase and Whipple*, 2012], differing vegetation cover [*Tucker and Slingerland*, 1997; *Acosta et al.*, 2015], or differing thresholds to hillslope erosion [*Montgomery and Dietrich*, 1992]. Alternatively, the basin geometry and connectivity may buffer or temporarily block sediment movement, resulting in mismatches between the timing of external forcing

and sedimentary responses [e.g., *Meade*, 1982; *Fryirs et al*., 2007a; *Savi et al*., 2013; *Bracken et al*., 2015]. Intermontane basins like Humahuaca may be particularly susceptible to such phenomena, as tectonic deformation and variations in bedrock erodibility can lead to a juxtaposition of open valleys and narrow bedrock gorges, which in turn can critically influence sediment transport times [*Fryirs et al*., 2007b; *Cavalli et al*., 2013]. Local tectonic activity may be superimposed on any of these, triggering sudden mass movements or local river aggradation/incision.

To better understand the production and transport of sediment in the Humahuaca Basin and their possible relationships with climatic and tectonic forcing, we analyze sediments from the late Pleistocene fill terraces and from the modern tributary channels. Specifically, we (1) expand the existing chronology on the timing of sediment aggradation and incision with new optically stimulated luminescence and cosmogenic ^{10}Be exposure ages, (2) investigate changes in erosion rates over time using ^{10}Be, and (3) evaluate grain size dependencies in the ^{10}Be-derived catchment mean erosion rates as a proxy for changes in erosion processes. We show how detailed dating and an analysis of erosion processes can help to distinguish among various potential forcing factors and determine what aspects of the system are most important in controlling the landscape response to that forcing.

2. Tectonic, Geomorphic, and Climatic Setting of the Humahuaca Basin

The intermontane Humahuaca Basin lies within the Eastern Cordillera of the southern Central Andes along the eastern margin of the Puna Plateau, which is the southern sector of the Altiplano-Puna Plateau (Figure 1). Near the latitude of the Humahuaca Basin (22.5–24°S), deformation affected the Eastern Cordillera during the Miocene-Pliocene, dividing the formerly contiguous foreland into a series of intermontane basins that are separated by local range uplifts (reviewed in *Strecker et al*. [2007, 2009]). Eastward propagating deformation uplifted the eastern side of the Humahuaca Basin (the Tilcara ranges) between 6 and 4.2 Ma [*Pingel et al*., 2013, 2014]. Basement rocks exposed along the basin-bounding ranges include the Late Proterozoic to early Palaeozoic low-grade metasediments of the Puncoviscana Formation [*Turner*, 1960; *Omarini*, 1983; *Aparicio González et al*., 2014], which are rich in centimeter-scale quartz veins. These units are superseded by Cambro-Ordovician sandstones and quartzites of the Mesón and Santa Victoria groups [*Moya*, 1988; *Sánchez and Salfity*, 1999; *Aceñolaza*, 2003], and the Late Cretaceous to Palaeogene Salta Group, which includes red fluvial sandstone and siltstones and white marine sandstones and carbonates [*Salfity*, 1982; *Galliski and Viramonte*, 1988; *Marquillas et al*., 2005]. Overlying the basement rocks in the Humahuaca Basin are (1) deformed sequences of variably consolidated, late Miocene to Pliocene conglomerates and sandstones, with remnants exposed in a 2 to 3 km wide swath along the lowermost slopes on the west side of the valley [*Kühn*, 1923; *Castellanos*, 1950; *Marshall et al*., 1982; *Salfity et al*., 1984; *Walther et al*., 1998; *Pingel et al*., 2013] and (2) conglomeratic Pleistocene terrace fills along tributary valleys that commonly exceed 100 m in thickness and are several kilometers in length [*Tchilinguirian and Pereyra*, 2001; *Robinson et al*., 2005; *Sancho et al*., 2008; *May and Soler*, 2010; *Pingel et al*., 2013]. Deformation has continued at least through the late Pleistocene within the basin, as documented by several tens of meters of offset of the late Pleistocene fills along thrust faults on both sides of the valley [*Sancho et al*., 2008; *Pingel et al*., 2013; *Streit et al*., 2015] and by folding of Pleistocene basin strata [*Salfity et al*., 1984; *Marrett et al*., 1994; *Sancho et al*., 2008; *Pingel et al*., 2013].

The deformation history and bedrock lithology have left distinct signatures in the tributary valley morphology and sedimentation patterns. While most of the western tributaries are oriented perpendicular (E-W) to the valley trunk stream (the southward flowing Río Grande), the eastern tributaries extend only a short distance upstream from the trunk stream through narrow bedrock gorges (in places only a few meters wide) before turning sharply to the north or south (Figures 2 and 3). There are commonly meter-scale boulders wedged within the gorges (Figure 3d). Differences in river steepness (k_{sn}) values are also prominent, with a dominance of very low values in the east (despite a wide spread of values) contrasting with more moderate values and a more limited range in the west (Figure 2c). The upper, N-S oriented reaches of the eastern tributary channels occupy perched sedimentary basins (Figures 3a and 3b). We have not estimated the volumes of the sediment in the perched basins, but they appear to be significantly larger than the volumes of the downstream fill terraces (e.g., Figure 3b). The sediment in the perched basins is similar to that in fill terraces at the tributary junctions with the valley trunk stream: poorly sorted layers of several centimeters to decimeters thickness that are dominated by subrounded to subangular clasts with scarce layers of sand. Locally, the fills

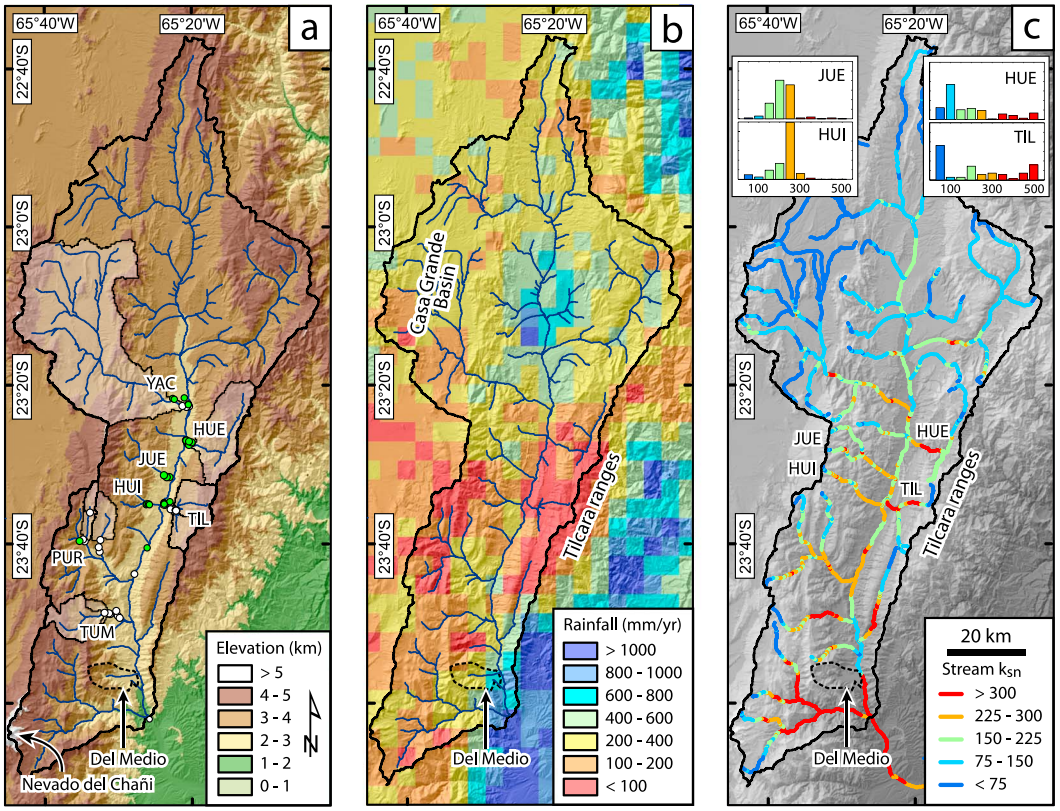

Figure 2. Topography, precipitation, and river steepness maps of the Humahuaca Basin. (a) Digital elevation model from Shuttle Radar Topography Mission (SRTM) data. White circles show ^{10}Be sample locations; green circles show OSL sample locations. Subcatchments in white shading show areas draining to sample locations. For zoomed view with each sample labeled, see supporting information Figure S1. YAC: Yacoraite; HUE: Huerta; TIL: Tilcara; JUE: Juella; HUI: Huichaira; PUR: Purmamarca; and TUM: Tumbaya. (b) Yearly rainfall from TRMM2B31 data calibrated to rain-station data [*Bookhagen and Strecker*, 2008]. (c) Normalized river steepness index (k_{sn}) values calculated with a reference concavity of 0.45. Normalized histograms in the upper part of the panel illustrate the distribution of k_{sn} values for two catchments each on the west and east sides of the valley (same abbreviations as in Figure 2a); colors in the histograms correspond to those shown in the legend.

consist of (1) organized sequences of tabular, bedded, imbricated pebble, and cobble conglomerates that fine upward into thin horizons of granule-sized material, representing unconfined sheet flood and less common channelized flow deposits and (2) matrix-supported boulder conglomerate horizons interbedded with the clast-supported imbricated pebble and cobble conglomerate horizons representing alluvial fan deposition with debris flows, mud flows, and sheet flood deposits.

The high topography of the Tilcara ranges on the eastern flank of the Humahuaca basin forms an orographic barrier to easterly moisture-bearing winds and separates the basin from the humid foreland to the east [*Bookhagen and Strecker*, 2008]. Within the Humahuaca Basin, rainfall is similar on the western and eastern valley flanks, ranging mostly from ~40 to 600 mm yr^{-1} (Figure 2b). Pleistocene glaciations have only affected the 5930 m high Nevado del Chañi, in the southernmost portion of the basin (Figure 2a). Although the general rainfall pattern has probably existed since the early Pliocene following uplift of the Tilcara ranges [*Pingel et al.*, 2014], significant millennial-scale variations in precipitation have been inferred nearby from paleolake studies on the Puna Plateau [*Bobst et al.*, 2001; *Godfrey et al.*, 2003; *Quade et al.*, 2008] and the Bolivian Altiplano [*Baker et al.*, 2001; *Fritz et al.*, 2004; *Placzek et al.*, 2006]. Over the last 50 to 70 ka, wetter climate periods (compared to today) have coincided with insolation maxima [*Baker et al.*, 2001; *Bobst et al.*, 2001; *Fritz et al.*, 2004], and as such may be at least partly coupled with the intensity of the South American Monsoon System (SAMS) [*Fritz et al.*, 2004] and associated increased easterly moisture transport [*Ammann et al.*, 2001; *Godfrey et al.*, 2003]. The orbital control is less pronounced prior to 70 ka [*Bobst et al.*, 2001; *Fritz et al.*, 2004; *Placzek et al.*, 2006]. Variations in precipitation likely affected the Humahuaca Basin as well, as enhanced contrast in the heating of the Southern and Northern Hemisphere associated with higher intensity

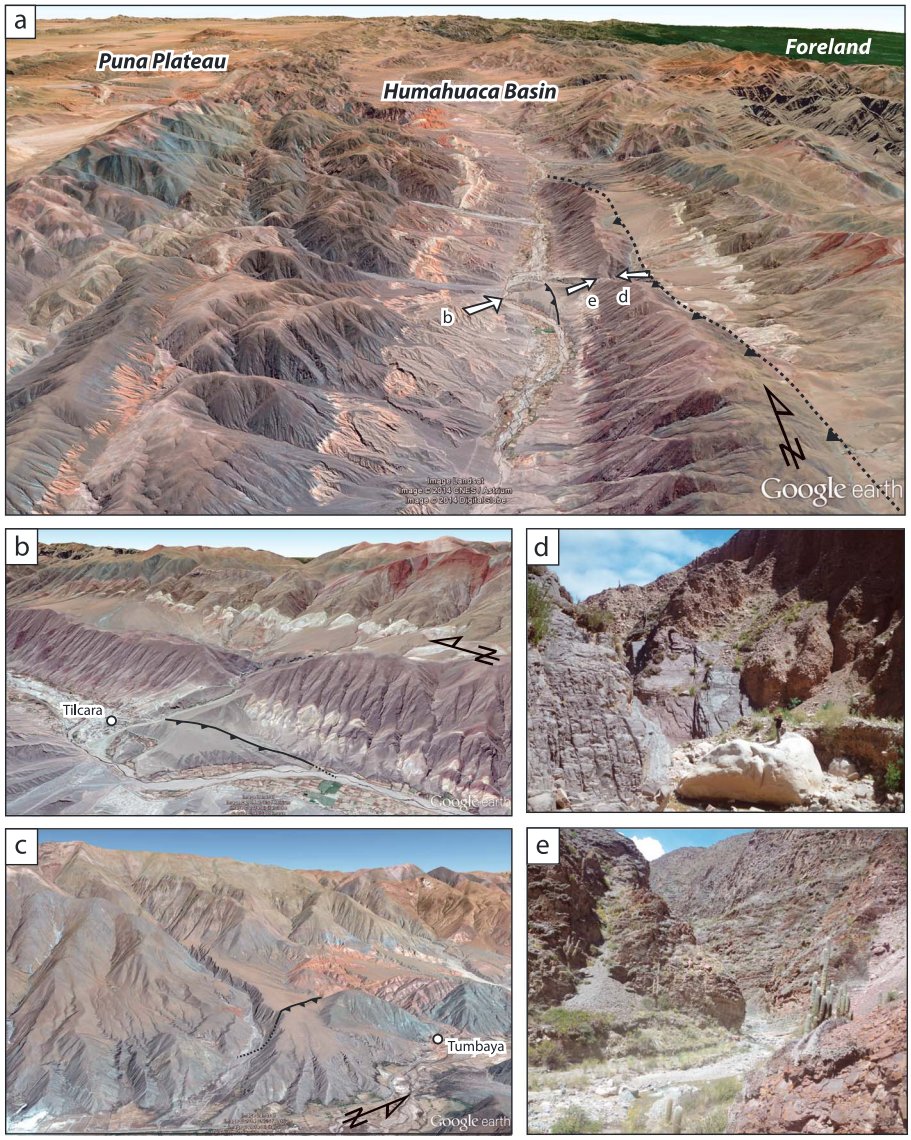

Figure 3. Google Earth images and field photos illustrating differences in catchment morphology on the western and eastern sides of the Humahuaca Basin. (a) Overview of basin, looking NW. The thrust fault that is dashed is buried; the one with the solid line has been active since the late Pleistocene. (b) Tilcara tributary with upstream perched basin. Fault cuts the late Pleistocene fill terrace. (c) Tumbaya tributary with thrust fault cutting the late Pleistocene terrace. (d) Tilcara gorge with large boulder (person standing on boulder for scale), facing downstream. (e) Outlet of Tilcara gorge, looking upstream.

of the SAMS drives strengthened upper air easterlies, providing more moisture to the Eastern Cordillera and the Altiplano-Puna [*Garreaud et al.*, 2003; *Vera et al.*, 2006; *Boers et al.*, 2013]. Convective storms in the Humahuaca region are also influenced by the South Atlantic Convergence Zone (SACZ) [*Vera et al.*, 2006; *Barros et al.*, 2000; *Boers et al.*, 2015], with a strengthened and northward displaced SACZ associated with greater precipitation in NW Argentina [*Barros et al.*, 2000].

3. Methods

3.1. OSL Dating of Fill Terrace Sediments

We used optically stimulated luminescence (OSL) to date the timing of sediment deposition within the fill terraces. Bleaching of sediment prior to burial ensures that any measured luminescence (residual stored charge) from environmental radiation is related to the time since burial. Partial bleaching is known to affect fluvial

deposits [*Murray and Olley*, 2002; *Wallinga et al*., 2002; *Spencer et al*., 2003; *Thomsen et al*., 2007; *Rittenour*, 2008; *Arnold and Roberts*, 2009; *Rhodes*, 2011] and is often a concern in depositional settings proximal to the source area, where sediment transport time is short. *Robinson et al*. [2005] suggested that four main facies achieve bleaching in these environments, and they were targets for our OSL sampling: thin, laterally discontinuous windblown deposits on the top of coarse-grained fluvial bars; laterally continuous or locally pervasive loess horizons; medium-grained, medium to well sorted fluvial bar-top and chute-channel fill deposits; and medium to coarse-grained alluvial fan sheet-flow deposits. Samples were collected in black PVC tubes and environmental radiation (related to U, Th, and K concentrations) was measured in situ for 30 min using an EG&G ORTEC MicroNOMAD gamma spectrometer. Samples were collected from both depth profiles and from exposed walls of the terraces to ensure that samples span the full range of aggradation periods. Details of sample preparation procedures in the laboratory and analyses can be found in the supporting information.

3.2. Cosmogenic Exposure Dating and Erosion Rates

We measured the concentration of the cosmogenic nuclide ^{10}Be in quartz to determine exposure ages of the terraces, catchment mean erosion rates from modern sediment and fill terrace sediment, and bedrock erosion rates. Although concentrations of ^{10}Be in sediment provide "denudation" rates (the removal of mass by physical and chemical weathering processes), we employ the more commonly used term "erosion" [*Summerfield*, 1991]. Because most of the bedrock in the basin is characterized by the quartz vein-rich Puncoviscana Formation and the sandstones and quartzites of the Mesón Group, the region is well suited to measuring ^{10}Be. Details of sample preparation techniques in the laboratory and accelerator mass spectrometry analysis for the ^{10}Be samples can be found in the supporting information.

We collected depth profiles of ^{10}Be samples consisting of between 2 and 9 samples within the upper 2 m of terrace surfaces to constrain their exposure age and the inherited nuclide concentration (nuclides accumulated prior to deposition [*Anderson et al*., 1996]). Depth profiles were dug into stable, undisturbed, subhorizontal surfaces away from terrace margins and far from surrounding higher topography that might lead to periodic or sustained surface burial. Profiles on the west side of the valley include YAC (Yacoraite tributary), TUM (Tumbaya tributary), PUR (Purmamarca tributary), and Pit5 (Yacoraite tributary). Pit1, Pit2, Pit3, and Pit4 are on the east side at the outlet of the Río de la Huerta valley ("HUE" in Figure 2). The locations at Río de la Huerta were selected atop distinct fill units whose surfaces lie at different elevations, with Pit1 sampling the highest (presumably stratigraphically oldest) unit and Pit2, Pit3, and Pit4 sampling successively lower units. Exact depth profile locations are shown in Figure S1 in the supporting information. Samples from depth profiles YAC, TUM, and PUR consisted of amalgamations of 40 to 50 pebbles between 1 and 4 cm diameter, while those of Pit1 through Pit5 consisted of 40 to 50 clasts between 5 and 10 cm diameter.

To estimate the inherited concentration of ^{10}Be and to calculate a terrace exposure age, we used the Monte Carlo simulator created by *Hidy et al*. [2010]. In running the simulations, we assumed a range of densities of 1.6 to 2.0 g cm^{-3} (results only differed by a few percent compared to a range of 1.6 to 1.8 g cm^{-3}) and an attenuation length scale of 160 ± 5 g cm^{-2}. On the terrace surfaces we sampled, there are commonly well-developed desert pavements, comprising a surface layer of tightly interlocked clasts overlying a layer of fine-grained sand and silt up to several decimeters thick. Such surfaces are commonly interpreted to have experienced inflation over time, with aeolian material accumulating beneath the uppermost layer of clasts, which are passively uplifted during the accumulation [e.g., *McFadden et al*., 1987; *Scherler et al*., 2014b]. To simulate inflation of those surfaces, we applied a constant negative erosion rate and a total (negative) erosion threshold equal to the thickness of the fine-grained unit. We excluded the surface sample from the simulation (as required by the simulator for inflating surfaces), but later used that sample to independently estimate a surface exposure age after subtracting the estimated inherited concentration. Nonconstant inflation may affect the calculated exposure age [e.g., *Scherler et al*., 2014b] but can be evaluated to a first order based on comparison with the exposure age derived from the surface sample. By default, the simulator calculates exposure ages based on a constant, site-specific production rate. Therefore, after running the simulator, we input the most probable surface concentration into the CRONUS online calculator version 2.2 [*Balco et al*., 2008] to determine the time-dependent "Lm" production rate over the approximately correct time interval. We then reran the Monte Carlo simulator with the time-dependent production rate to obtain a more accurate estimate of the exposure age and inherited concentration.

Table 1. OSL Results

Sample Name	ShortName	N^a	U(ppm)	Th(ppm)	K(ppm)	H_2O^b (%)	CosmicDose Rate^c ($mGya^{-1}$)	TotalDose Rate ($mGya^{-1}$)	D_e(Gyr)	MeanAge^d (ka)	MAMAge^e (ka)
HOR110204-77	HOR-77	34	2.15 ± 0.12	10.33 ± 0.30	1.76 ± 0.03	0.70	0.05	3.00 ± 0.15	97.2 ± 9.7	32.4 ± 3.6	n/a
HUE060303-29	HUE-29	16	1.91 ± 0.12	11.85 ± 0.32	1.54 ± 0.03	11.32	0.03	2.81 ± 0.15	218.2 ± 7.2	n/a	107.8 ± 9.4
HUE060303-30	HUE-30	46	2.25 ± 0.12	9.10 ± 0.28	1.53 ± 0.03	2.31	0.26	2.92 ± 0.16	103.8 ± 3.6	35.6 ± 2.3	n/a
HUE070303-31	HUE-31	88	2.76 ± 0.13	11.78 ± 0.32	2.25 ± 0.03	0.77	0.12	3.78 ± 0.16	240.9 ± 11.1	63.8 ± 3.9	n/a
HUE070303-32	HUE-32	13	2.12 ± 0.11	7.36 ± 0.25	1.09 ± 0.02	11.49	0.29	2.38 ± 0.16	172.0 ± 12.5	72.2 ± 7.1	n/a
HUE070303-33	HUE-33	28	1.90 ± 0.11	7.29 ± 0.25	1.19 ± 0.02	8.64	0.29	2.42 ± 0.16	217.2 ± 12.1	n/a	89.9 ± 7.7
HUE080803-34	HUE-34	23	2.22 ± 0.12	8.75 ± 0.28	1.16 ± 0.02	0.00	0.29	2.56 ± 0.16	92.8 ± 13.7	n/a	36.2 ± 5.8
HUE310104-57	HUE-57	19	2.69 ± 0.13	10.14 ± 0.30	1.72 ± 0.03	3.90	0.21	3.23 ± 0.16	303.6 ± 24.5	94.1 ± 8.9	n/a
HUE010204-60	HUE-60	35	2.09 ± 0.12	9.71 ± 0.29	1.79 ± 0.03	5.00	0.03	2.94 ± 0.15	218.0 ± 25.7	74.2 ± 9.6	n/a
HUE010204-61	HUE-61	10	2.23 ± 0.12	10.64 ± 0.31	1.80 ± 0.03	0.55	0.01	3.04 ± 0.15	247.4 ± 35.3	81.5 ± 12.3	n/a
HUE010204-62	HUE-62	24	2.03 ± 0.11	8.28 ± 0.27	1.55 ± 0.03	0.83	0.20	2.77 ± 0.15	232.0 ± 14.9	83.9 ± 7.2	n/a
HUE020204-64	HUE-64	31	1.88 ± 0.11	9.05 ± 0.28	1.54 ± 0.03	4.20	0.01	2.59 ± 0.15	146.8 ± 9.4	56.6 ± 4.9	n/a
HUE020204-65	HUE-65	16	2.42 ± 0.12	9.26 ± 0.28	1.65 ± 0.03	0.00	0.07	2.90 ± 0.15	294.3 ± 17.5	101.6 ± 8.1	n/a
HUI270104-47	HUI-47	80	2.01 ± 0.12	9.20 ± 0.28	1.91 ± 0.03	0.80	0.16	3.14 ± 0.15	128.6 ± 11.1	n/a	41.0 ± 4.1
HUI270104-48	HUI-48	46	2.17 ± 0.41	9.28 ± 0.95	1.90 ± 0.09	2.40	0.09	3.10 ± 0.19	159.0 ± 14.6	n/a	51.4 ± 5.7
HUI270104-49	HUI-49	48	2.51 ± 0.13	9.90 ± 0.29	2.15 ± 0.03	0.50	0.02	3.39 ± 0.15	184.8 ± 7.8	54.5 ± 3.4	n/a
HUI270104-50	HUI-50	48	1.83 ± 0.12	8.28 ± 0.29	1.61 ± 0.03	0.85	0.01	2.59 ± 0.15	153.6 ± 7.7	n/a	59.3 ± 4.6
JUE090303-37	JUE-37	12	2.11 ± 0.12	9.80 ± 0.29	1.51 ± 0.03	0.40	0.05	2.70 ± 0.15	175.9 ± 12.0	65.1 ± 5.8	n/a
JUE090303-38	JUE-38	12	1.97 ± 0.12	9.81 ± 0.29	1.73 ± 0.03	0.14	0.01	2.84 ± 0.15	119.7 ± 14.7	42.1 ± 5.7	n/a
JUE090303-39	JUE-39	23	1.90 ± 0.13	9.21 ± 0.25	1.77 ± 0.02	0.80	0.06	2.90 ± 0.15	135.5 ± 9.5	47.2 ± 4.2	n/a
TILC040303-21	TILC-21	26	2.48 ± 0.12	9.52 ± 0.29	2.06 ± 0.03	0.82	0.03	3.28 ± 0.15	275.8 ± 8.8	84.1 ± 4.8	n/a
TILC040303-22	TILC-22	20	2.38 ± 0.24	10.49 ± 0.52	2.20 ± 0.11	1.80	0.25	3.61 ± 0.18	248.5 ± 16.9	n/a	68.8 ± 5.8
TILC260104-44	TILC-44	36	2.38 ± 0.12	10.16 ± 0.30	2.14 ± 0.03	0.00	0.04	3.39 ± 0.15	245.9 ± 9.4	72.5 ± 4.3	n/a
YAC240303-02	YAC-02	24	2.17 ± 0.11	7.63 ± 0.26	1.32 ± 0.02	5.00	0.03	2.36 ± 0.15	107.7 ± 13.2	45.6 ± 6.3	n/a
YAC240303-03	YAC-03	56	1.52 ± 0.10	6.30 ± 0.23	1.17 ± 0.02	0.64	0.01	1.96 ± 0.15	225.7 ± 20.4	n/a	115.1 ± 13.7
YAC011303-42	YAC-42	49	1.80 ± 0.11	9.29 ± 0.28	1.60 ± 0.03	1.28	0.27	2.90 ± 0.16	288.3 ± 36.6	n/a	99.5 ± 13.7
YAC080303-35	YAC-35	29	1.44 ± 0.10	6.76 ± 0.24	0.99 ± 0.02	0.25	0.14	1.92 ± 0.15	107.6 ± 5.7	56.0 ± 5.4	n/a
YAC080303-36	YAC-36	43	1.96 ± 0.12	9.86 ± 0.29	1.40 ± 0.03	2.89	0.29	2.80 ± 0.16	70.4 ± 7.3	n/a	25.1 ± 3.0
YAC040204-67	YAC-67	43	1.82 ± 0.12	9.94 ± 0.29	1.48 ± 0.03	0.50	0.02	2.58 ± 0.15	122.9 ± 8.2	47.0 ± 4.3	n/a

[a]Number of replicated D_e estimates.
[b]Percent moisture compared to dry weight. Uncertainty taken as 5%.
[c]Cosmic dose rate calculated assuming constant burial depth using method described in *Prescott and Hutton* [1994]. Uncertainty taken as 10%.
[d]D_e and ages calculated using mean D_e.
[e]D_e and ages calculated using mean value of first age cluster from finite age model and the relative error (MAM) [*Galbraith et al.*, 1999].

To determine modern and paleo–catchment mean erosion rates [e.g., *Bierman and Steig*, 1996; *Granger et al.*, 1996; *von Blanckenburg*, 2005], we measured the concentration of ^{10}Be in samples of detrital sand and pebbles from modern channels and fill terraces in tributary catchments that range in size from 17 to 948 km^2 with mean slopes of 11.6 to 20.8° (Figures 2a and S1). From the modern channels, we collected samples at least several tens of meters away from any fill terraces. From the fill terraces, we collected samples from recently exposed walls that were at least several tens of meters below the terrace surface, and we dug ~50 cm into the wall before collection to avoid material with significant postdeposition nuclide accumulation. From the sand samples, we processed the 0.25 to 0.71 mm grain size fraction. The pebble samples consisted of 50 to 60 amalgamated pebbles with diameters of 1 to 3 cm. We calculated catchment mean, time-dependent ^{10}Be production rates using the approach described in *Scherler et al.* [2014a], which implements functions within TopoToolbox v2 [*Schwanghart and Scherler*, 2014]. Time-dependent production rates were calculated for each 90 m resolution pixel within the contributing drainage basin considering topographic shielding together with "Lm" latitude and elevation scaling (from *Lal* [1991] modified by *Stone* [2000]) as within CRONUS version 2.2 [*Balco et al.*, 2008]. For paleo-erosion rates, we calculated time-dependent production rates from the time of deposition [cf. *Scherler et al.*, 2015], based on either OSL samples collected in close proximity to the cosmogenic sample or on the surface exposure age of the terrace (Table 2). These production rates were averaged across the catchment and used to convert ^{10}Be concentrations into catchment mean erosion rates. When reporting uncertainties on those rates, we consider the "external" uncertainties, which include uncertainties in the reference ^{10}Be production rate for spallation and in the production rate

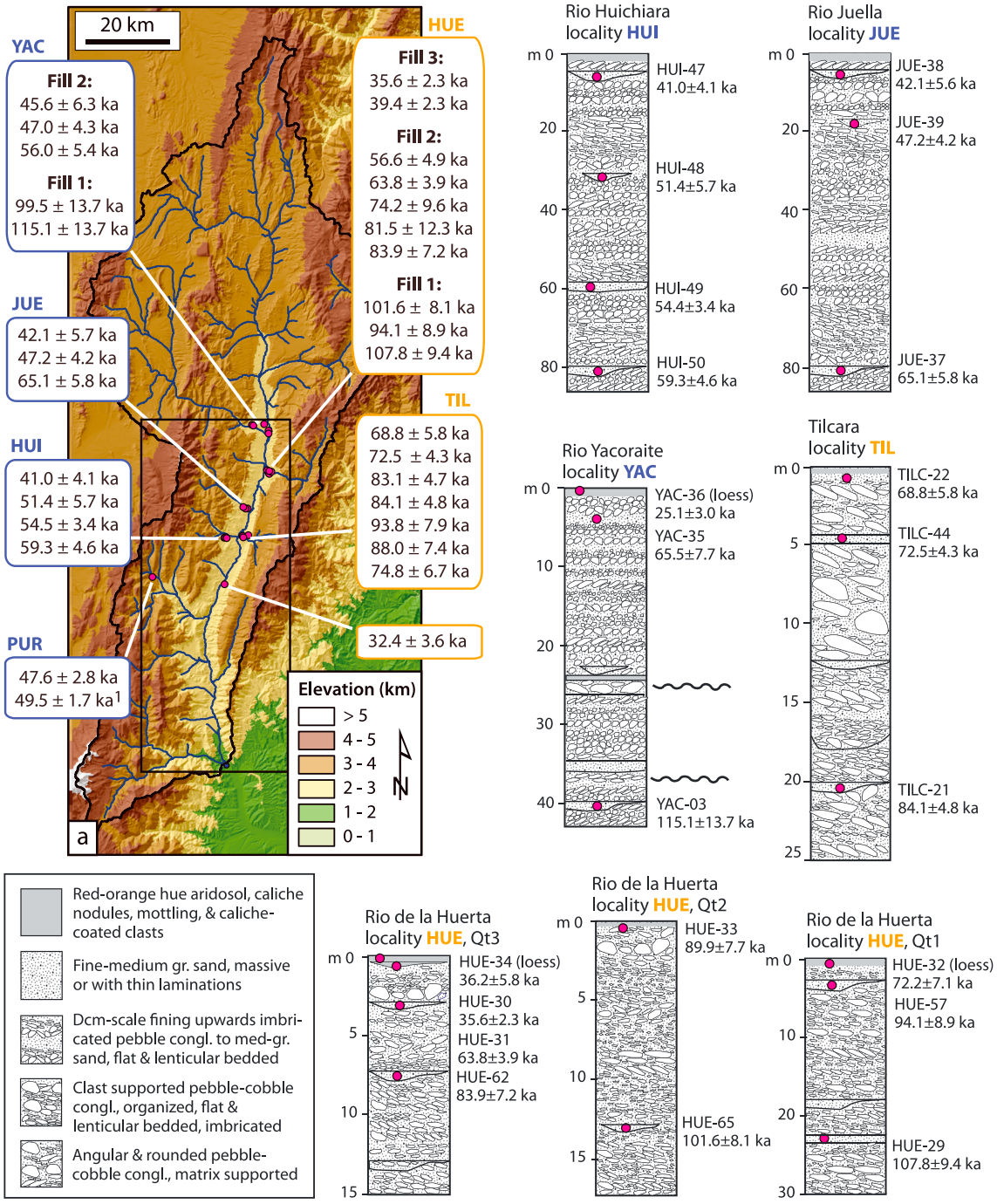

Figure 4. Sedimentological logs and OSL ages of alluvial fill units underlying the terraces. (a) OSL ages separated into western and eastern sides of the valley. Locations of the logs refer to locality names shown in Figure 4a. At Río de la Huerta, we label the highest fill unit, which we presume to be oldest, Qt1, with subsequently lower and presumably younger fills labeled Qt2 and Qt3. Magenta circles correspond to sample locations within the section. Black wavy lines in Yacoraite profile indicates an inferred discontinuity.

by muons [*Balco et al.*, 2008]. When reporting and discussing results in the text, we refer to 2σ uncertainty limits except where noted otherwise.

We also collected three bedrock samples to determine bedrock erosion rates from the tops of convex ridges. Those samples comprised material within the uppermost 3 cm of the bedrock surface. We calculated erosion rates with the CRONUS online calculator version 2.2 [*Balco et al.*, 2008] using the *Lal* [1991] scaling modified by *Stone* [2000] and time-dependent production rates (denoted Lm).

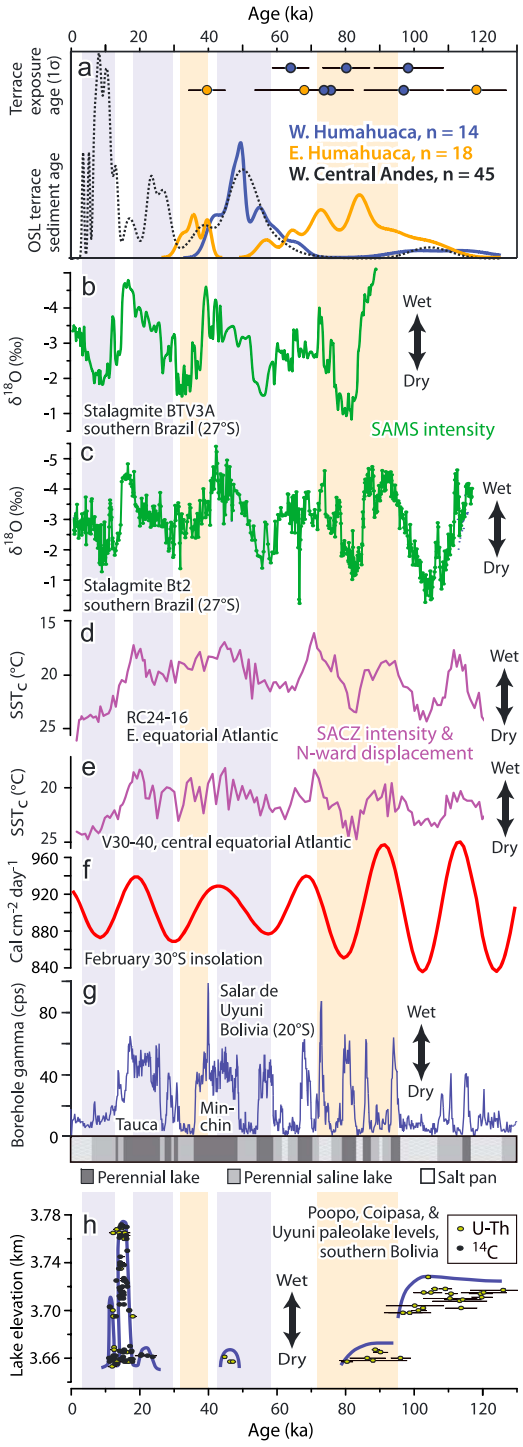

4. Results

4.1. Timing of Fill Terrace Aggradation and Abandonment

4.1.1. Fill Terrace Aggradation (OSL Ages)

Our new OSL dates (Table 1) in the Humahuaca Basin reveal terrace fill ages of ~32 to 115 ka, and ages of fine-grained material beneath the desert pavement surfaces of ~25 to 90 ka. We present representative OSL ages and uncertainties in radial plots, which simultaneously give a visual representation of data accuracy, precision and spread (Figure S2). Additional samples and ages of related units are listed in Table 1. Overall, the timing of aggradation on the west side of the Humahuaca Basin (14 samples) tends to differ from the east side (18 samples) (Figure 4). When plotted as cumulative probability distribution functions, the peaks in ages are distinct between ~32 and 90 ka but are difficult to distinguish earlier, due to the larger uncertainties in ages and/or the limited number of samples older than 90 ka (Figure 5).

The four dated fine-grained deposits beneath the desert pavement surfaces (Figure 4 and Table 1) yield ages that are younger than the exposure ages of the surfaces below which they were sampled (see section 4.1.2), consistent with the notion that material is aeolian and inflated the surfaces. As such, we do not consider those dates to represent the timing of fluvial aggradation, and we do not plot them in Figure 5.

Figure 5. Compilation of OSL dates of terrace sediment and terrace ^{10}Be exposure ages compared to paleoclimate records. (a) OSL dates are shown as stacked probability density functions with the number of samples (*n*) indicated. Dashed black line from western Andes (data from *Steffen et al.* [2009, 2010]), orange line from east side of Humahuaca, blue line from west side of Humahuaca. Beryllium-10 exposure ages are shown as colored circles (west side in blue, east side in orange). (b) Oxygen isotope record from stalagmite BTV3A (Batuverá Cave, southern Brazil, see Figure 1c for location) from *Wang et al.* [2007]. (c) Oxygen isotope record from stalagmite Bt2 (also Batuverá Cave) from *Cruz et al.* [2005]. (d and e) Sea surface temperature records [from *McIntyre et al.*, 1989] are minimum (i.e., cold) values, hence labeled SST_C. (f) Variations in both stable isotope and SST records are interpreted to be dominantly controlled by insolation, as illustrated in the record from *Berger and Loutre* [1991]. (g) Gamma ray record from Salar de Uyuni from *Fritz et al.* [2004]. (h) Paleolake highstands on the Bolivian Altiplano from *Placzek et al.* [2006]. In blue and orange shading, we highlight periods where aggradation on the western and eastern sides of the valley appears not to overlap.

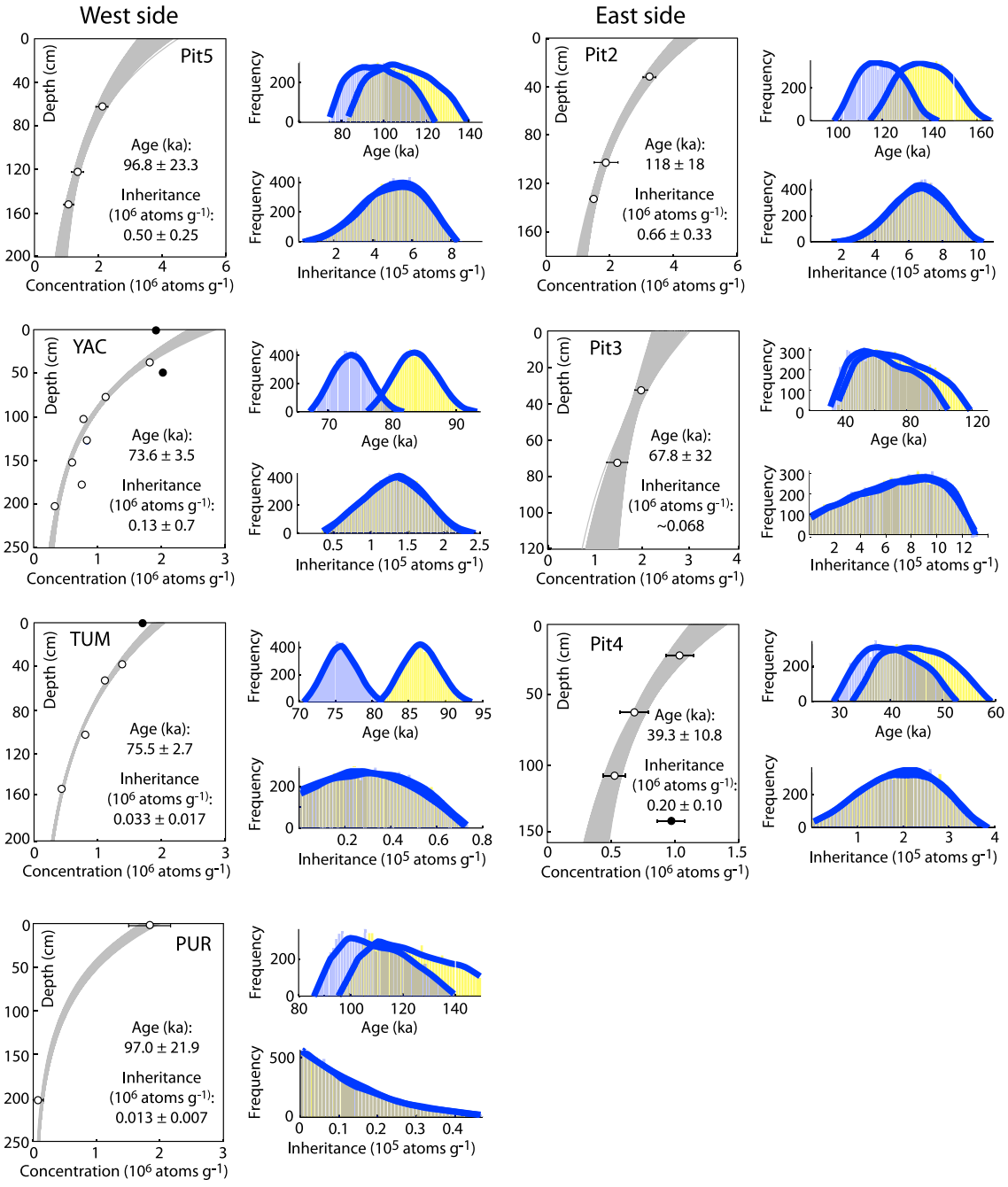

Figure 6. Monte Carlo simulation results of cosmogenic depth profiles. Samples shown with white circles were included in the simulation; those shown with black circles were not. Errors plotted are 2σ. Frequency plots to the right of the depth-concentration plots illustrate simulator results using a constant production rate (colored yellow) and using a time-dependent production rate (colored blue). In our interpretations, we only consider the results derived from the time-dependent production rate.

A few locations where we obtained multiple OSL dates from individual fill units reveal ages that are in correct stratigraphic order; these ages help to constrain time spans and rates of aggradation. In the Río Huichaira and Juella tributary valleys on the west side of the Humahuaca Basin, OSL dates over ~75 m of stratigraphic thickness (Figure 4) reveal similar aggradation rates of 4.3 ± 1.4 m kyr^{-1} from ~59 to 41 ka and 3.4 ± 1.1 m kyr^{-1} from ~65 to 42 ka, respectively (using *York et al.* [2004] regressions). On the east side of the valley, a slower aggradation rate of 1.4 ± 0.6 m kyr^{-1} occurred at Tilcara from ~84 to 69 ka. Also on the east side, aggradation rates of 0.14 ± 0.03 m kyr^{-1} from ~84 to 36 ka, 1.0 ± 1.0 m kyr^{-1} from ~102 to 90 ka, and 1.5 ± 1.4 m kyr^{-1} from

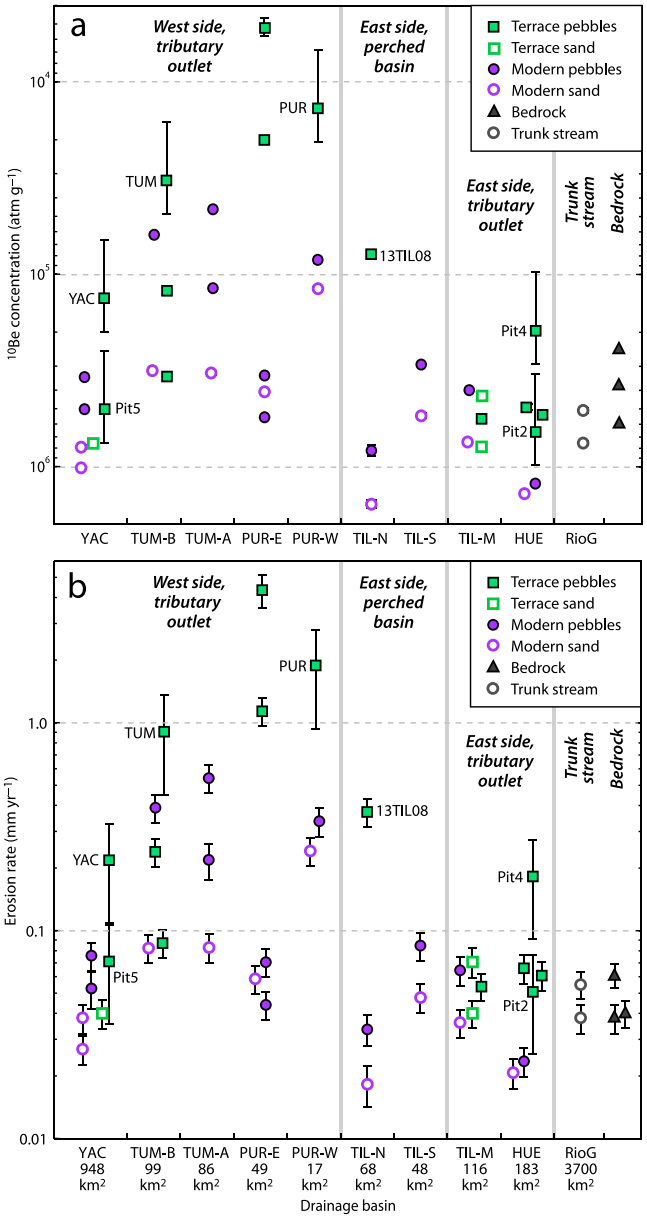

Figure 7. Cosmogenic nuclide sample (a) ^{10}Be concentrations and (b) erosion rates from modern rivers, fill terraces, and bedrock ridges. Where error bars are not visible, the uncertainties are smaller than the plotted symbols. The two samples from the trunk stream are from *Bookhagen and Strecker* [2012]. Inherited concentration and erosion rates from depth profiles are labeled with the profile name (Pit2, Pit4, Pit5, YAC, and TUM). Samples are divided into west side tributay outlets, east side perched basins, and east side tributary outlets. Uncertainties plotted are 2σ. First three letters of catchment abbreviations at bottom correspond to labels in Figure 2a. YAC: Yacoraite; HUE: Huerta; TIL-N: Tilcara, northern tributary; TIL-S: Tilcara, southern tributary; TIL-M: Tilcara, main branch; PUR-E: Purmamarca, east; PUR-W: Purmarca, west; TUM-B: Tumbaya, below tributary confluence; and TUM-A: Tumbaya, above tributary confluence.

108 to 94 ka are recorded at Río de la Huerta. While these sections generally start near the base of the exposed fills, we cannot constrain how much aggraded material lies beneath the present channels.

4.1.2. Cosmogenic Depth Profiles: Terrace Abandonment and ^{10}Be Inheritance

All but one of our depth profiles yielded exponentially decreasing concentrations with depth that allowed us to determine both exposure ages and inherited concentrations of ^{10}Be. In our Monte Carlo simulations for depth profiles YAC, PUR, and TUM, the small analytical uncertainties together with probable natural scatter in the data (due to, for example, variable inheritance) preclude finding fits at a 2σ analytical uncertainty level. A more complex aggradation/exposure history may provide better fits, but uncertainties on the final calculated exposure age would remain large. Instead, we used the lowest chi-square limit that permitted the simulator to find fits. For surface exposure ages, we report Bayesian probability limits. For nuclide inheritance, we report the mean value with an estimated 2σ uncertainty of 50% of the mean value based on the frequency distribution of values (Figure 6). For consistency, we use the same convention for all depth profiles.

On the west side of the valley, depth profiles YAC and Pit5 were collected from the Yacoraite terrace. The three samples of Pit5 yielded a most probable age of 96.8 ± 11.7 ka and a mean inherited concentration of $50.4 \pm 25.2 \times 10^4$ atoms g^{-1} (Figure 6 and Table S3). To find reasonable fits for the YAC profile, one outlier sample was excluded (depth of 50 cm). The remaining samples yielded a Bayesian most probable age of 73.6 ± 1.7 ka and mean inherited concentration of $13.2 \pm 6.6 \times 10^4$ atoms g^{-1} (Figure 6 and Table S3). The exposure age calculated for the surface sample (63.8 ± 5.5 ka, 1σ) agrees within 2σ uncertainty limits. Four samples from the TUM depth profile on the west side of the valley yielded an exposure age of 75.5 ± 1.3 ka and mean inherited concentration of

Table 2. Modern and Paleo-Erosion Rates From Detrital Samples and Depth Profiles

Sample	Description	Sample Latitude (°S)	Sample Longitude (°W)	Mean Slope (°)	Basin Area (km^2)	Mean Elevation[c] (m)	Measured ^{10}Be Concentration[d] (10^3 atm g^{-1}, 1σ)	ErosionRate[e] (mm yr^{-1}, 1σ)	ErosionRate[f] (mm yr^{-1}, 1σ)	Unit Age[g] (ka)
					Yacoraite					
YAC[a]	Terrace qtzt pebbles	−23.3775	−65.3430	12.3	948	3835	132.4±33.10	0.187±0.047	0.218±0.055	75[2]
Pit5[a]	Terrace clasts	−23.3780	−65.3403	12.3	948	3835	503.8±126.0	0.053±0.013	0.071±0.01775	95[2]
12YAC03	Terrace sand	−23.3776	−65.3444	12.3	948	3835	755.5±6.796	0.036±0.003	0.040±0.003	75[2]
12YAC05	Modern qtzt pebbles	−23.3795	−65.3463	12.3	948	3835	342.4±3.887	0.076±0.006	-	-
12YAC06	Modern qtz pebbles	−23.3795	−65.3463	12.3	948	3835	502.4±6.242	0.053±0.005	-	-
12YAC07	Modern sand	−23.3795	−65.3463	12.3	948	3835	1014.1±7.411	0.027±0.002	-	-
STR-23[b]	Modern sand	-23.3772	-65.3553	12.6	946	3830	791.8±8.900	0.039±0.003	-	-
					Purmamarca (East)					
12PUR01-A	Modern qtz pebbles	−23.6589	−65.5423	18.4	49	3623	553.2±4.947	0.044±0.003	-	-
12PUR01-B	Modern qtzt pebbles	−23.6589	−65.5423	18.4	49	3623	335.8±3.004	0.070±0.005	-	-
12PUR01-C	Modern sand	−23.6589	−65.5423	18.4	49	3623	407.9±3.135	0.059±0.005	-	-
12PUR02	Terrace coarse sand	−23.6834	−65.5440	18.4	49	3623	20.04±0.300	1.079±0.082	1.135±0.086	50[1]
12PUR03	Terrace qtzt pebbles	−23.6740	−65.5460	18.4	49	3623	5.221±0.283	4.195±0.385	4.358±0.402	50[1]
					Purmamarca (West)					
12PUR04	Modern sand	−23.6012	−65.5661	20.5	17	4199	118.8±1.069	0.242±0.019	-	-
12PUR05	Modern qtzt pebbles	−23.6012	−65.5661	20.5	17	4199	84.21±1.487	0.335±0.026	-	-
PUR[a]	Terrace qtzt pebbles	−23.6618	−65.5778	20.8	33	3884	13.40±3.350	1.986±0.497	1.833±0.508	97[2]
					Tumbaya (Below Confluence With Tributary)					
TUM[a]	Terrace qtzt pebbles	−23.8177	−65.5028	19.1	99	3834	32.50±8.125	0.737±0.184	0.908±0.115	75[2]
12TUM04	Modern sand	−23.8144	−65.5197	19.1	99	3834	317.0±2.806	0.082±0.006	-	-
12TUM05	Modern qtzt pebbles	−23.8144	−65.5197	19.1	99	3834	62.32±0.649	0.389±0.030	-	-
12TUM06	Terrace qtzt pebbles	−23.8126	−65.5224	19.1	99	3834	121.7±1.260	0.205±0.016	0.240±0.019	75[2]
12TUM07	Terrace qtzt pebbles	−23.8126	−65.5224	19.1	99	3834	339.3±3.362	0.077±0.006	0.087±0.007	75[2]
					Tumbaya (Above Confluence With Tributary)					
12TUM02	Modern sand	−23.8115	−65.5326	18.5	86	3918	326.0±3.624	0.083±0.007	-	-
12TUM03	Modern qtzt pebbles	−23.8115	−65.5326	18.5	86	3918	118.1±1.400	0.219±0.022	-	-
12TUM03B	Modern qtz pebbles	−23.8115	−65.5326	18.5	86	3918	45.97±0.529	0.541±0.041	-	-
					Huacalera					
13HUE01	Modern sand	−23.4552	−65.3350	17.6	183	3936	1383±11.13	0.021±0.002	-	-
13HUE02	Modern qtzt pebbles	−23.4552	−65.3350	17.6	183	3936	1224±16.12	0.024±0.002	-	-
13HUE03	Terrace pebbles	−23.4501	−65.3454	17.6	183	3936	491.9±9.037	0.057±0.005	0.066±0.005	80[1]
13HUE04	Terrace qtzt pebbles	−23.4501	−65.3454	17.6	183	3936	537.1±8.972	0.052±0.004	0.061±0.005	80[1]
Pit2[a]	Terrace pebbles	−23.4544	−65.3430	17.6	183	3936	657.2±164.3	0.043±0.011	0.051±0.007	118[2]
Pit4[a]	Terrace pebbles	−23.4495	−65.3459	17.6	183	3936	195.2±48.93	0.135±0.034	0.183±0.04575	40[2]
					Tilcara (Main Stem)					
13TIL01	Terrace sand	−23.5859	−65.3947	16.3	116	3794	425.4±4.811	0.061±0.005	0.071±0.006	80[1]
13TIL02	Terrace sand	−23.5859	−65.3949	16.3	116	3794	787.9±10.14	0.034±0.003	0.040±0.003	80[1]
13TIL03	Terrace pebbles	−23.5859	−65.3949	16.3	116	3794	565.8±7.664	0.047±0.004	0.054±0.004	80[1]

Table 2. (continued)

Sample	Description	Sample Latitude (°S)	Sample Longitude (°W)	Mean Slope (°)	Basin Area (km^2)	Mean Elevation[c] (m)	Measured ^{10}Be Concentration[d] (10^3 atm g^{-1}, 1σ)	ErosionRate[e] (mm yr^{-1}, 1σ)	ErosionRate[f] (mm yr^{-1}, 1σ)	Unit Age[g] (ka)
13TIL04	Modern sand	−23.5936	−65.3825	16.3	116	3794	744.0±8.395	0.036±0.003	-	-
13TIL05	Modern qtzt pebbles	−23.5936	−65.3825	16.3	116	3794	400.2±5.676	0.065±0.005	-	-
					Tilcara (Northern Tributary)					
13TIL06	Modern qtzt pebbles	−23.5958	−65.3712	15.0	68	3839	826.0±25.11	0.034±0.003	-	-
13TIL07	Modern sand	−23.5958	−65.3712	15.0	68	3839	1568±34.61	0.018±0.002	-	-
13TIL08	Terrace qtzt pebbles	−23.5962	−65.3716	15.0	68	3839	78.98±1.513	0.310±0.024	0.372±0.029	80[1]
					Tilcara (Southern Tributary)					
13TIL09	Modern sand	−23.5963	−65.3720	18.4	48	3750	543.9±8.376	0.048±0.004	-	-
13TIL10	Modern qtzt pebbles	−23.5963	−65.3720	18.4	48	3750	294.9±4.692	0.085±0.007	-	-
					Bedrock Erosion Rates					
12PUR08	Puncoviscano (qtz)	−23.6577	−65.5818	-	-	3205	598.4±5.291	0.038±0.003	-	-
12TUM08	Meson Group (qtzt)	−23.8222	−65.4983	-	-	2445	379.9±3.429	0.040±0.003	-	-
12TUM09	Puncoviscano (qtz)	−23.8075	−65.5062	-	-	2455	244.3±2.169	0.061±0.004	-	-
					Rio Grande					
STR-21[b]	Modern sand	−24.0346	−65.4302	15.5	5903	3670	755.5±10.17	0.038±0.003	-	-
STR-24[b]	Modern sand	−23.7301	−65.4648	13.8	4427	3730	511.1±8.450	0.055±0.004	-	-

[a]Erosion rate calculated from the best fit inherited concentration of the depth profile following Monte Carlo simulations.
[b]Sample published in *Bookhagen and Strecker* [2012].
[c]Catchment mean elevation for detrital samples, local sample site elevation for bedrock samples
[d]Blank-corrected values. Blank uncertainty propagated into total uncertainty.
[e]Erosion rates calculated with time-dependent production rate assuming all samples have zero age.
[f]Erosion rates calculated with time-dependent production rate based on the age of the deposit (see text for details).
[g]Age assumed to be zero for modern samples; terrace sample age based on nearby OSL/^{14}C date (1) or ^{10}Be exposure age (2).

$3.3 \pm 1.7 \times 10^4$ atoms g^{-1} (Figure 6 and Table S3). The exposure age calculated from the surface sample (80.0 ± 6.9 ka, 1σ) agrees within 1σ uncertainty limits. The two-sample profile at PUR yielded an exposure age of 97.0 ± 21.9 ka and a mean inherited concentration of $1.34 \pm 0.7 \times 10^4$ atoms g^{-1} (Figure 6 and Table S3).

On the east side of the valley near the outlet of Río de la Huerta valley, Pit2 and Pit4 yielded three consecutive samples showing decreasing concentrations with depth. They resulted in Bayesian most probable ages of 118 ± 8.7 ka (Pit 2) and 39.3 ± 5.4 ka (Pit4), and mean inherited ^{10}Be concentrations of $65.7 \pm 32.8 \times 10^4$ atoms g^{-1} (Pit 2) and $19.6 \pm 9.8 \times 10^4$ atoms g^{-1} (Pit 4) (Figure 6 and Table S3). From Pit3, the top two samples show decreasing concentrations with depth, but the bottom sample shows a higher concentration. After excluding the lowermost sample, we found a Bayesian most probable age of 67.8 ± 14 ka and a mean inherited concentration of $\sim 68 \times 10^4$ atoms g^{-1} (with a larger uncertainty compared to the other pits, Figure 6). Despite the larger uncertainties associated with the Pit3 results, the age is in the correct presumed stratigraphic order, and the mean inherited concentration is within the same order of magnitude as Pit2 and Pit4. Pit1 yielded a more variable pattern of ^{10}Be concentrations with depth (Table S2), which is inadequate to constrain an exponential trend.

4.2. Catchment Mean and Bedrock Erosion Rates

The ^{10}Be concentrations that we measured for our modern and terrace sediment detrital samples span three orders of magnitude, from $\sim 5 \times 10^4$ to 1568×10^4 atoms g^{-1}. Overall, for individual catchments, the pebble samples yield lower concentrations compared to sand, and the catchments on the west side yield a much wider range of concentrations compared to those in the east (Figure 7a). We discuss these patterns in more detail after converting the concentrations to erosion rates (Figure 7b).

4.2.1. Modern Erosion Rates

From the modern channels, sand samples yield catchment mean erosion rates ranging from ~0.02 to 0.24 mm yr^{-1}, while pebble samples yield rates ranging from ~0.02 to 0.54 mm yr^{-1} (Table 2). Uncertainties

(1σ) range from ~7 to 11%. Overall, rates are higher on the west side, with sand averaging 0.09 mm yr^{-1} and pebbles averaging 0.22 mm yr^{-1}, versus 0.03 mm yr^{-1} for sand and 0.05 mm yr^{-1} for pebbles on the east side (Figure 7b). When comparing results for a single catchment, pebbles generally (with only one exception) yield higher mean erosion rates compared to sand (Figure 7b). Two previously published sand samples taken from near the Humahuaca Basin outlet yielded erosion rates of 0.038 ± 0.006 mm yr^{-1} (sample STR-21) and 0.055 ± 0.008 mm yr^{-1} (sample STR-24) [*Bookhagen and Strecker*, 2012]. Those rates are similar to the three bedrock erosion rates, which range from 0.038 ± 0.006 to 0.061 ± 0.008 mm yr^{-1} (2σ, Table 2 and Figure 7b).

4.2.2. Paleo-Erosion Rates From Fill Terrace Sediments

Sand layers are uncommon within the fill terraces, so most of our paleo-erosion rates are derived from pebbles or from our estimates of inherited ^{10}Be concentrations in the depth profiles (Table 2). Although we present the paleo-erosion rates assuming both a zero age and a measured age of the deposit (Table 2), we only discuss the latter rates. We present the zero-age rates solely to illustrate the importance of correcting for the sediment age for some samples, as differences between the two rates range from ~3 to 35%.

On the west side of the valley, paleo-erosion rates span 2 orders of magnitude, from ~0.04 to 4.4 mm yr^{-1}, which often greatly exceed and sometimes overlap with modern erosion rates (Table 2 and Figure 7b). In contrast, on the east side of the valley, paleo-erosion rates largely overlap with erosion rates from modern samples, with rates below or within uncertainty of 0.1 mm yr^{-1} (Figure 7b). One exception to this pattern on the east side is the relatively high pebble paleo-erosion rate of 0.37 ± 0.03 mm yr^{-1} from the perched basin upstream from the bedrock gorge in Tilcara (13TIL08, Figure 7b). We assumed an age of 80 ka for that deposit to calculate the paleo-erosion rate (similar to the aggradation age of the fill downstream); however, the age of the sediment within the perched basin is unknown. Nonetheless, alternative late Pleistocene ages also result in higher erosion rates compared to the zero-age estimate of 0.31 ± 0.02 mm yr^{-1} (Table 2), which itself is still well above the other rates from the east side.

5. Discussion

5.1. Sediment Aggradation and Incision Cycles in the Humahuaca Basin

The terrace exposure ages on the west side are all older than the peak in OSL dates, whereas on the east side, one exposure age predates the broad, older peak in OSL ages and the two younger exposure ages fall between the two peaks of OSL ages (albeit the large age uncertainties make precise comparisons difficult) (Figure 5). Although we expect to find terrace exposure ages that postdate the OSL ages (surface exposure postdates aggradation), the lack of younger exposure ages could relate to our sampling strategy. We targeted the central portions of the terraces for depth profiles to minimize the likelihood of surface erosion. Because even the terraces with simple morphology may comprise multiple periods of filling and incision, our depth profile sampling would have been biased toward older generations of fills. OSL samples, in contrast, were most often collected from incised walls of the terrace fills along the modern channels, where younger units are more likely exposed. Despite this potential bias in our sampling, differences in the timing of aggradation and incision on the western and eastern sides of the valley based on OSL ages are prominent, and point to multiple, antiphased periods of aggradation and incision along the tributary valleys. This antiphased timing in turn implies that the triggers for the main aggradation phases are likely to have arisen within the tributary valleys themselves, rather than being a response to aggradation along the trunk stream (the Río Grande).

With respect to late Pleistocene regional paleoclimate records, on the west side of the Humahuaca Basin, aggradation coincided with periods of increasing intensity of the South American Monsoon System (SAMS), which is marked by decreasing δ^{18}O in stalagmites from southern Brazil (Figure 5) [*Cruz et al.*, 2005; *Wang et al.*, 2007]. There are no millennial-scale climate archives that directly record variations in the South Atlantic Convergence Zone (SACZ). Nonetheless, modern rainfall anomalies in NW Argentina are associated with a strengthened and northward displaced SACZ [*Barros et al.*, 2000; *Boers et al.*, 2015], phenomena that tend to occur together and are associated with negative sea surface temperature (SST) anomalies in the equatorial Atlantic [*Barros et al.*, 2000]. Those negative SST anomalies in turn are correlated with enhanced easterlies [*McIntyre et al.*, 1989; *Molfino and McIntyre*, 1990] and show strong positive correlations with periods of high insolation over the past 200 ka [*McIntyre et al.*, 1989; *Molfino and McIntyre*, 1990; *Schneider et al.*, 1995]. The correlation between the peak in OSL dates on the west side of the valley and decreasing SSTs in the

equatorial Atlantic (Figure 5; note the reversed SST axes) therefore points toward aggradation during increasing intensity and northward displacement of the SACZ. The timing of aggradation on the west side also corresponds to the earlier part of the interval of perennial paleolakes in southern Bolivia [*Fritz et al*., 2004] and a documented high lake level in Laguna Pozuelos on the Puna between 43 and 37 ka [*McGlue et al*., 2013]. As such, aggradation on the west side occurred during periods of increasing precipitation in the region.

Conversely, on the east side of the Humahuaca Basin, the young peak in OSL ages (~30 to 40 ka) overlaps with periods of decreasing intensity of the SAMS, decreasing intensity and southward displacement of the SACZ, and with a declining phase of the perennial Bolivian paleolakes (Figure 5). The older, broader peak in ages encompasses periods of both increasing and decreasing intensities of the SAMS and SACZ, and corresponds to more variable conditions, when precessional control on precipitation on the plateau was apparently less strong [*Bobst et al*., 2001; *Fritz et al*., 2004; *Placzek et al*., 2006]. Lake levels, nonetheless, experienced an overall decline (Figure 5). While it is difficult to relate this older peak in ages to specific paleoclimate conditions, aggradation on the east side appears to have occurred mainly during decreasing or variable precipitation conditions.

The peak in ages on the west side of the valley from ~40 to 60 ka corresponds to a peak in OSL ages from fill terraces in the western Central Andes (Figure 5 and Table S1). Both that peak and an additional, younger peak in ages in the western Andes from circa 20 to 30 ka are coeval with increasing intensity of the SAMS (Figure 5 and Table S1). Although the Holocene peak in ages has also been suggested to relate to climate forcing, the specific climatic phenomenon that affected the region remains unclear [*Steffen et al*., 2009, 2010]. Overall, this comparison with paleoclimate records illustrates that aggradation in both the western Central Andes and the western side of Humahuaca Basin occurred during increasing precipitation, while aggradation on the eastern side of Humahuaca occurred during decreasing or more variable precipitation.

5.2. Cosmogenic Nuclide Evidence for Landslides and Mass Movements

Both theoretical and field studies have demonstrated that cosmogenic nuclide concentrations measured from multiple samples collected over time or from different sediment sizes can reveal information about sediment production and transport processes [e.g., *Brown et al*., 1995, 1998; *Matmon et al*., 2003; *Belmont et al*., 2007; *Aguilar et al*., 2014; *Carretier et al*., 2015]. Mass movements can mobilize material from several meters beneath the surface, which leads to a short-term pulse of sediment with low concentrations of cosmogenic nuclides [e.g., *Brown et al*., 1995; *Savi et al*., 2014; *Olen et al*., 2015]. Although such localized mobilization of low-concentration material violates the steady state erosion assumption required to convert detrital sediment nuclide concentrations into meaningful catchment mean erosion rates, it provides a potential signature of mass wasting processes. Numerical modeling studies have illustrated that due to the stochastic nature of landslides, detrital sediment samples in landslide-prone regions should yield a wide range of cosmogenic erosion rates that may underestimate or overestimate true catchment mean erosion rates, particularly from smaller basins [*Niemi et al*., 2005] without significant sediment storage [*Yanites et al*., 2009]. A similar rationale explains how nuclide concentrations from different sediment sizes can be sensitive to landslide activity: because landslides preferentially mobilize larger grain sizes from greater depths below the surface compared to diffusive hillslope processes, grain size dependency in the nuclide concentrations (with lower concentrations in larger grain sizes) may be diagnostic of landslide activity [e.g., *Brown et al*., 1995, 1998]. Several field studies in landslide-prone regions have provided support for this inference [e.g., *Brown et al*., 1998; *Belmont et al*., 2007; *Aguilar et al*., 2014; *McPhillips et al*., 2014; *Puchol et al*., 2014]. We use these concepts to investigate the importance of landslides based on our cosmogenic nuclide samples from the modern channels and the fill terraces, specifically focusing on grain size dependence and variability in the calculated erosion rates.

5.2.1. Landslide Signatures in Modern Samples

Hillslopes in the region show widespread evidence for gullying and mass movements (Figures 3 and S3). As a result, we can examine the cosmogenic nuclide data from modern samples to gauge if our samples are sensitive to mass movements. Erosion rates from the tributary sand samples mostly fall between 0.02 and 0.1 mm yr^{-1} (Figure 7b). This range broadly overlaps with the erosion rates measured on sand samples from the Río Grande, whose large drainage area (~3700 km^2) should make the samples relatively insensitive to landslides [*Niemi et al*., 2005; *Yanites et al*., 2009], and it overlaps with rates from the convex bedrock ridges, which appear to be unaffected by sudden mass wasting processes. Based on the overlapping rates, we infer that the sand samples from the tributaries are also minimally affected by landslides. One exception is the

higher erosion rate of 0.24 ± 0.02 mm yr^{-1} for the sand sample 12PUR04. Its upstream catchment is the smallest within our sample set (17 km^2), which could imply that it has less effective mixing compared to the other samples and hence is more sensitive to landslides or gullying [*Niemi et al*., 2005].

The amalgamated pebble samples from both the eastern and western tributaries consistently yield higher erosion rates compared to sand collected in the same location (with only one exception: 12PUR01-A) (Figure 7b). Many of the erosion rates from pebbles also exceed the rates measured on the convex bedrock ridges and the trunk stream samples (Figure 7b), which are less sensitive to landslides. Because mass wasting processes are active on modern hillslopes (Figure S3), our cosmogenic nuclide results support previous inferences that larger grain sizes may record landslide activity and that grain size dependencies in erosion rates may provide a proxy for the importance of mass movements as a hillslope process [*Brown et al*., 1998; *Belmont et al*., 2007; *Aguilar et al*., 2014; *McPhillips et al*., 2014; *Puchol et al*., 2014].

5.2.2. Landslide Signatures in Fill Terrace Samples

Our cosmogenic samples collected from the fill terrace sediments give us perspective into how both paleo-erosion rates and hillslope processes have changed over time, as they record the cosmogenic signatures of the sediment at the time of deposition. Because the terrace fill on the west side aggraded during periods of increasing precipitation and on the east side during periods of decreasing precipitation, the cosmogenic data reflect processes occurring over different time periods on each side of the valley.

Our paleo-erosion rates show differences on the western and eastern sides of the basin that may reflect differing degrees of landslide activity in the past (Figure 7b). On the west side of the valley, pebble samples yield a wide range of paleo-erosion rates, spanning 2 orders of magnitude from 0.05 to 4.4 mm yr^{-1}. These highly variable (and often very high) rates likely reflect an increased importance of landslides at the time when the terraces were aggrading compared to today. As noted, on the west side of the valley, aggradation occurred during increasing precipitation (Figure 5). In contrast, on the east side of the valley, the paleo-erosion rates based on pebbles largely overlap with those from modern sediments from the tributaries, modern sediments from the trunk stream, and with erosion rates from the bedrock ridges (Figure 7b). This pattern indicates that landslide activity today is similar to the time when the channels were aggrading, which was a time of decreasing or variable precipitation.

There are two exceptions to this pattern. Sample 13TIL08 on the east side shows a relatively high pebble paleo-erosion rate of 0.37 ± 0.03 mm yr^{-1}, well above the range of modern rates on that side of the valley (Figure 7b). That sample was collected from the perched basin upstream from the bedrock gorge in Tilcara, hinting at potentially greater past landslide activity within the perched basin. Unfortunately, due to a lack of appropriate material for OSL or ^{14}C dating, we do not have a depositional age on the sediment within the perched basin. Another exception is the Yacoraite catchment ("YAC" in Figure 7), which shows a range of paleo-erosion rates similar to those on the east side. We discuss a possible explanation for that behavior in section 5.3.3.

5.3. External and Internal Controls on Sediment Transport and Aggradation

The antiphased timing of fill terrace formation on the western and eastern sides of the Humahuaca Basin is intriguing with respect to potential forcing mechanisms. Although the link between wetter climate periods and a greater importance of landslides on the west side of the Humahuaca Basin appears well documented with our data, the absence of coeval, landslide-related fill deposits on the east side is enigmatic at first. We consider next how changes in the balance between sediment supply and transport capacity, tectonics, and valley geometry/connectivity may have influenced the timing and location of fluvial aggradation.

5.3.1. Changes in Sediment Supply and Fluvial Transport Capacity

Aggradation occurs when fluvial systems have insufficient capacity to transport the sediment supplied from hillslopes [e.g., *Bull*, 1991]. In this section, we consider how temporal and spatial variations in both sediment supply and fluvial transport/incision might explain our observations from the Humahuaca Basin.

In general, sudden mass wasting events like landslides and debris flows increase sediment supply relative to transport capacity, triggering fluvial aggradation [e.g., *Miller and Benda*, 2000]. Aggradation has also been shown to occur during periods of increasing precipitation without sudden mass wasting: greater rainfall can lead to an expansion of the channel network, and the associated temporary increase in sediment supply can in turn trigger aggradation along the main channel [*Horton*, 1945; *Montgomery and Dietrich*, 1992; *Tucker*

and Slingerland, 1997]. On the other hand, both field [e.g., *Bull*, 1979; *Acosta et al*., 2015] and modeling studies [*Tucker and Slingerland*, 1997] have argued that when precipitation decreases, decreasing vegetation cover can trigger a temporary increase in sediment supply and consequent aggradation. These scenarios allow us to explain aggradation under either decreasing or increasing precipitation conditions due to changes in sediment supply. However, the rock types, vegetation cover, and mean slopes on the west and east sides of the Humahuaca Basin are all very similar. Hence, it is difficult to explain why the west side might be more sensitive to mass wasting or an expansion of the drainage network, while the east side is more sensitive to changes in vegetation cover.

Variations in precipitation over time will affect runoff and the transport capacity of river systems. To explain the observations from Humahuaca Basin, we must consider how it may be possible for the west and east sides to respond differently to the same climate shift. One possibility would involve differences in the threshold for erosion along river systems, which would affect their sensitivity to storm frequency: areas with high erosion thresholds would only experience incision during large storm events [e.g., *Tucker and Bras*, 2000; *Molnar*, 2001; *Tucker*, 2004; *Lague et al*., 2005; *Molnar et al*., 2006; *DiBiase and Whipple*, 2012]. Although the bedrock lithology is similar on both sides of the valley, implying a similar erosion threshold, the low river steepness values in the upper portions of the tributaries on the east side of the valley (Figure 2c) would require a higher critical discharge to overcome a given erosion threshold (see discussion in *DiBiase and Whipple* [2012]). The intriguing implication is that if drier periods are stormier, areas with differing erosion thresholds or channel steepnesses could respond differently to a change in climate: high-threshold, low-steepness channels would preferentially incise during stormier times (even if mean precipitation is lower), whereas low-threshold, high-steepness channels would preferentially incise during wetter times (even if they are less stormy) [*Molnar*, 2001; *Molnar et al*., 2006; *DiBiase and Whipple*, 2012]. We have no direct records of storminess during the late Pleistocene. Nonetheless, the timing of incision and aggradation is opposite of what we would predict in this particular scenario. Aggradation (rather than incision) occurs in the lower steepness eastern side during times of decreasing precipitation, and aggradation occurs in the higher-steepness western side during times of increasing precipitation.

Following these arguments, it is difficult to find a reason for the differences in the timing of aggradation and incision on the western and eastern sides of the valley only considering changes in hillslope sediment supply and river transport capacity. We next consider how tectonic activity or landscape connectivity may influence sediment supply and transport.

5.3.2. Tectonic Influence on Sediment Cycles

Various tectonic processes may influence sediment flux. Large earthquakes can trigger landslides and create plugs of sediment that migrate through fluvial systems [e.g., *Dadson et al*., 2004]. Considering the timescale of disturbance to the sediment flux following an earthquake is typically less than a decade where it has been studied in Taiwan, Papua New Guinea, and Japan [*Dadson et al*., 2004; *Hovius et al*., 2011; *Marc et al*., 2015], repeated large earthquakes would be required to produce prolonged aggradation. Even if the response timescale is longer in more arid environments, repeated disturbances are likely needed to produce the fill terraces in Humahuaca Basin that aggraded over tens of kiloyears. In the eastern Central Andes, there is no precedent for seismic activity producing extensive landslides, nor is there evidence that seismicity has differed on either side of the Humahuaca Basin (both sides have been deformed in the late Pleistocene). Also, landslides today are well correlated with years of high annual rainfall [*Paolini et al*., 2005]. Although we cannot reconstruct earthquake activity in the past, the increased importance of landslides during a past period of increasing precipitation and the relatively long duration of aggradation points to a climatic rather than seismic trigger for landslides in the area.

Alternatively, changes in drainage-divide positions related to tectonic activity or other processes could influence sediment flux, leading to river incision or aggradation [*Bishop*, 1995]. The relatively high relief of the basin margins throughout the area implies that over late Pleistocene timescales, if there have been shifts in drainage divides, they are likely to have been limited to the areas close to the divides. One exception is the upper Yacoraite catchment, where the elevated, low-relief Casa Grande Basin (Figure 2b) appears to have only recently been captured by the Yacoraite river. In fact, sediment provenance and stratigraphy shows that the basin was fully isolated between 2.1 and $<$1.7 Ma due to uplift along its eastern margin but was recaptured by 0.8 Ma [*Streit et al*., 2015].

Finally, deformation along alluvial rivers induced by fault movement can trigger incision and the formation of terraces in regions with steepened slopes, or aggradation in areas of decreased slope [e.g., *Ouchi*, 1985]. The

excavation of the Pliocene and younger basin fill has been suggested to have triggered multiple episodes of fault reactivation within the Humahuaca Basin [*Pingel et al*., 2013]. Indeed, fault movement has induced several tens of meters of vertical offset of the late Pleistocene terraces on both the east and west sides of the valley (Figures 3b and 3c) [*Sancho et al*., 2008; *Pingel et al*., 2013]. This fault movement (in both cases, the thrusts verge upstream) could have temporarily dammed the tributaries and induced upstream aggradation, while uplifted sediments in the hanging walls were incised. However, there are no fill terraces of more than a few meters height (above the active channel) that are either synchronous with or postdate this fault activity. Considering that these clearest demonstrations of late Quaternary fault movement have produced only very small terraces, it is difficult to invoke local fault movement to explain the formation of the large (>100 m thick) fill terraces along the tributary valleys.

It is less certain whether periodic storage in the perched sedimentary basins on the east side (Figure 3a) could relate to fault activity. Theoretically, uplift along the east-verging thrust buried beneath the perched basin fill (Figure 3a) could have temporarily dammed the drainage system, until overtopping sediment and subsequent outflow could carve a new gorge into the uplifted bedrock ridge and reestablish a downstream connection. However, the damming of significant volumes of sediment would require tens of meters of offset, with the basement overriding Pleistocene sediment. Considering that we see no evidence for such a relationship in the field and that the timing of aggradation on the east side is directly out of phase with past increases in precipitation, we favor a climate-related mechanism for the damming.

5.3.3. Differing Valley Geometry and Connectivity

Differing valley geometry and connectivity on either side of the Humahuaca Basin may offer an alternative explanation for our observations. If storminess did not increase during past dry phases and landslides were just as likely to occur in the east as in the west (as we argued above), landslides were likely triggered throughout the Humahuaca Basin during periods of increasing precipitation. In this case, on the west side of the valley, sediment mobilized by mass movements would aggrade within the tributary valleys, particularly near their downstream outlets. On the east side of the valley, in contrast, coeval aggradation in the near the tributary outlets did not occur. One possible explanation is that voluminous, sudden pulses of coarse sediment (e.g., debris flows) dammed the narrow bedrock gorges at the downstream outlets of the perched sedimentary basins (Figures 3d and 3e), forcing most of the sediment to accumulate upstream (Figure 8a). Later, during periods of decreasing precipitation when landslide activity was reduced, material that dammed the narrow bedrock gorges would have been slowly removed. Sediment in the perched sedimentary basins would in turn be slowly excavated, transferred downstream, and deposited where the valley width increases near the intersection with the main valley (Figure 8b). The excavation process would provide time for the sediments stored within the perched basins to accumulate more ^{10}Be prior to their redeposition in the fill terraces, which could mask or even eliminate any cosmogenic nuclide landslide signature that may have existed in the perched basin sediments [e.g., *Yanites et al*., 2009]. In the model that emerges, fill terraces downstream from the narrow bedrock gorges on the east side would tend to be out of phase with the climate forcing that drives mass movements, lack a clear ^{10}Be landslide signature, and have experienced slower aggradation compared to the west side. All of these predictions are consistent with our observations. This model may also explain why the Yacoraite catchment on the west side, with the large, low-relief Casa Grande Basin in its upstream reaches, shows a cosmogenic signature similar to that of the east side. Although this model remains speculative, we emphasize that even if transient storage alone tends to smooth out grain size dependencies in cosmogenic nuclide concentrations and delay sediment transfer downstream, blocking of the gorges by landslides or debris flows explains why downstream aggradation on the east side only occurred when precipitation was decreasing.

5.4. Sedimentary Records of Landscape Response to Climate Change

Our results are consistent with previous studies linking late Pleistocene fill terraces in the Central Andes to orbitally forced climate shifts [*Steffen et al*., 2009, 2010; *Bekaddour et al*., 2014]. Our data point to fluvial aggradation during times of increasing precipitation within drainage basins with a relatively simple morphology along the west side of Humahuaca Basin. Previous studies from the western Andes associated aggradation with wetter climate periods [*Steffen et al*., 2009, 2010]. However, our comparison of the western Andean data to paleoclimate proxy records (Figure 5) indicates that the western Andean sites in fact experienced aggradation during times of increasing precipitation, rather than during peak precipitation. Together, this work from the Central Andes supports previous inferences that transient changes in climate have the most

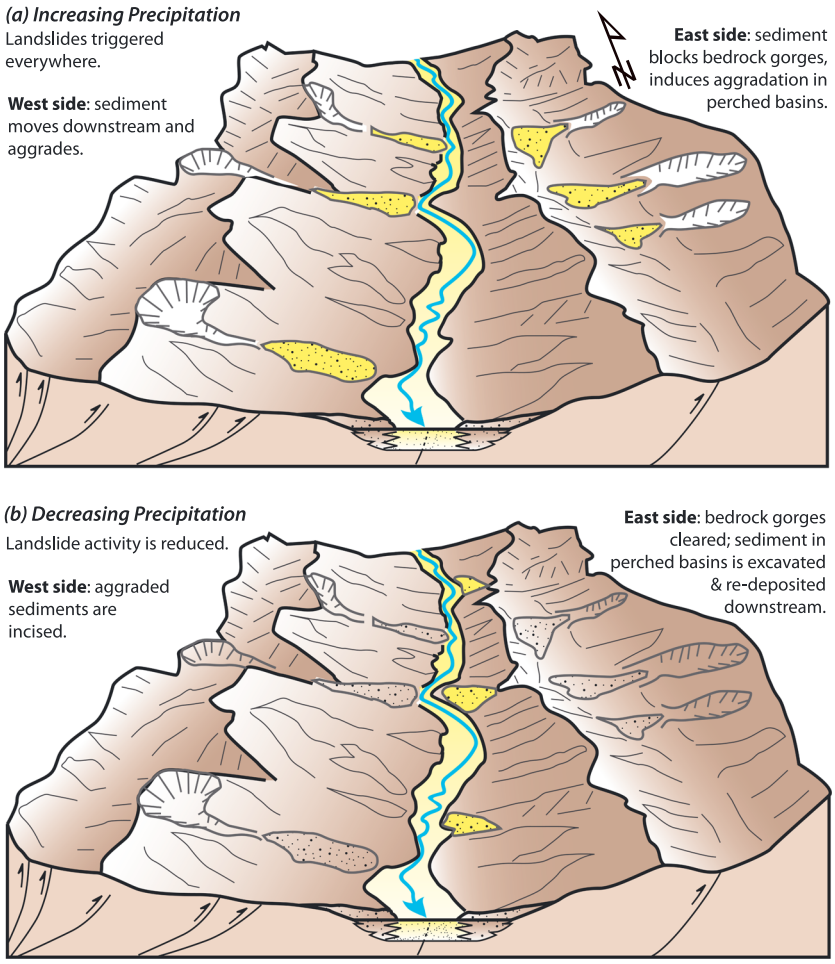

Figure 8. Cartoon illustrating sediment mobilization from shallow landslides and differing timing of deposition in fill terraces along the western and eastern sides of the valley. (a) We suggest that landslides triggered by increasing precipitation block the narrow bedrock gorges at the downstream end of the perched sedimentary basins on the east side, leading to sediment deposition in the perched basins. (b) In times of decreasing precipitation, the gorges on the east side become cleared of sediment, and sediment moves from the perched basins downstream to the tributary outlets.

substantial impacts on landscapes with respect to erosion and sediment transport [*Donnelly*, 1982; *Bull*, 1991; *Tucker and Slingerland*, 1997; *Inman and Jenkins*, 1999; *Zhang et al*., 2001; *Molnar*, 2004].

Unlike within the geometrically simple basins on the west side of Humahuaca, the timing of aggradation on the east side, where narrow bedrock gorges facilitate damming by landslides or debris flows, correlates with periods of decreasing precipitation. If we are correct in inferring that this valley geometry (with narrow bedrock gorges) is a primary factor leading to the antiphased timing of downstream sediment delivery, then larger basins that integrate areas with both well and poorly connected sediment routing geometries should have an attenuated response to climate forcing with respect to sediment flux. Similar inferences have been drawn from a modeling study of sediment flux through landscapes with different degrees of morphological complexity, with greater complexity leading to larger mismatches between hillslope erosion and sediment discharge at the outlet [*Baartman et al*., 2013].

6. Conclusions

Within the Humahuaca Basin of NW Argentina, our OSL ages of terrace sediments illustrate that aggradation along tributaries on the west side of the valley primarily occurred during late Pleistocene periods of increasing precipitation and on the east side during periods of decreasing or variable precipitation. Our cosmogenic ^{10}Be data show that although landsliding is an important process today for mobilizing sediment from

hillslopes, it was even more important during past periods of aggradation on the west side of the valley (when precipitation was increasing). On the east side, the pattern is more complex, with a possible signature of landsliding in the upper perched basins but no increased importance of landslides during the downstream aggradation (when precipitation was decreasing).

Differences in valley geometry and connectivity can explain this diachroneity in aggradation. Landslides were likely triggered throughout the landscape when the climate was becoming wetter. We envision that the mobilization of sediment from landslides led to aggradation in the western tributaries but to blockage of the narrow bedrock gorges along the eastern tributaries. Later, as precipitation decreased, those blockages were slowly removed, resulting in the remobilization of dammed sediment in the east and its redeposition in downstream fill terraces. By integrating our data with previously published data from the western Central Andes, it appears as if across this broad zone of arid to semiarid climates, fluvial aggradation peaked during times of increasing precipitation, unless it was influenced by transient sediment storage. Overall, our data illustrate how landscape connectivity can influence the timing of sediment evacuation from tributary valleys, with both in-phase and out-of-phase responses to climate forcing within a relatively small region.

Acknowledgments

All OSL and cosmogenic nuclide data plotted in the figures can be found in the data tables and the supporting information, whereas paleoclimate data used to produce Figure 5 can be obtained from the cited references. This work was funded by the Emmy Noether Programme of the Deutsche Forschungsgemeinschaft (DFG) grant SCHI 1241/1-1 awarded to T. Schildgen, awards from the Petroleum Research Fund and the Carnegie Trust to R. Robinson, and a DFG Leibniz Award to M. Strecker (DFG 373/18-1). We thank Eric Kirby, Heiko Pingel, Brian Clarke, and Jean Dixon for discussions that helped inspire this work. Detailed and constructive reviews from three anonymous reviews, Editor John Buffington, and AE Nicole Gasparini helped to improve the depth and clarity of our manuscript.

References

Aceñolaza, G. F. (2003), The Cambrian system in Northwestern Argentina: Stratigraphical and palaeontological framework, *Geol. Acta*, *1*(1), 23–39.

Acosta, V. T., T. F. Schildgen, B. A. Clarke, D. Scherler, B. Bookhagen, H. Wittmann, F. von Blanckenburg, and M. R. Strecker (2015), Effect of vegetation cover on millennial-scale landscape denudation rates in East Africa, *Lithosphere*, *7*, 421–426.

Aguilar, G., S. Carretier, V. Regard, R. Vassallo, R. Riquelme, and J. Martinod (2014), Grain size-dependent ^{10}Be concentrations in alluvial stream sediment of the Huasco Valley, a semi-arid Andes region, *Quat. Geochron.*, *19*, 163–172.

Ammann, C., B. Jenny, K. Kammer, and B. Messerli (2001), Late Quaternary glacier response to humidity changes in the arid Andes of Chile (18–29°S), *Palaeogeogr. Palaeoclimatol. Palaeoecol.*, *172*, 313–326.

Anderson, R. S., J. L. Repka, and G. S. Dick (1996), Explicit treatment of inheritance in dating depositional surfaces using in situ ^{10}Be and ^{26}Al, *Geology*, *24*(1), 47–51.

Aparicio González, P. A., M. M. Pimentel, N. Hauser, and M. Cristina Moya (2014), U-Pb ICP-MS geochronology of detrital zircon grains from low grade metasedimentary rocks (Neoproterozoic-Cambrian) of the Mojotoro Range, northwestern Argentina, *J. South Am. Earth Sci.*, *49*, 39–50.

Arnold, L. J., and R. G. Roberts (2009), Stochastic modeling of multi-grain equivalent dose (D-e) distributions: Implications for OSL dating of sediment mixtures, *Quat. Geochronol.*, *4*(3), 204–230.

Baartman, J. E. M., R. Masselink, S. D. Keesstra, and A. J. A. M. Temme (2013), Linking landscape morphological complexity and sediment connectivity, *Earth Surf. Processes Landforms*, *38*(12), 1457–1471.

Baker, P. A., C. A. Rigsby, G. O. Seltzer, S. C. Fritz, T. K. Lowenstein, N. P. Bacher, and C. Veliz (2001), Tropical climate changes at millennial and orbital timescales on the Bolivian Altiplano, *Nature*, *409*, 698–701.

Ballato, P., A. Landgraf, T. F. Schildgen, D. F. Stockli, M. Fox, M. R. Ghassemi, E. Kirby, and M. R. Strecker (2015), The growth of a mountain belt forced by base-level fall: Tectonics and surface processes during the evolution of the Alborz Mountains, N Iran, *Earth Planet. Sci. Lett.*, *425*, 204–218.

Balco, G., J. O. Stone, N. A. Lifton, and T. J. Dunai (2008), A complete and easily accessible means of calculating surface exposure ages or erosion rates from ^{10}Be and ^{26}Al measurements, *Quat. Geochronol.*, *3*, 174–195.

Barros, V., M. Gonzáles, B. Liebmann, and I. Camilloni (2000), Influence of the South Atlantic convergence zone and South Atlantic sea surface temperature on interannual summer rainfall variability in southeastern South America, *Theor. Appl. Climatol.*, *67*, 123–133.

Beaumont, C., P. Fullsack, and J. Hamilton (1992), Erosional control of active compressional orogens, in *Thrust Tectonics*, edited by K. R. McClay, pp. 1–18, Springer, Netherlands.

Bekaddour, T., F. Schlunegger, H. Vogel, R. Delunel, K. P. Norton, N. Akçar, and P. Kubik (2014), Paleo erosion rates and climate shifts recorded by Quaternary cut-and-fill sequences in the Pisco valley, central Peru, *Earth Planet. Sci. Lett.*, *390*, 103–115.

Belmont, P., F. J. Pazzaglia, and J. C. Gosse (2007), Cosmogenic ^{10}Be as a tracer for hillslope and channel sediment dynamics in the Clearwater River, western Washington State, *Earth Planet. Sci. Lett.*, *264*(1), 123–135.

Berger, A., and M. F. Loutre (1991), Insolation values for the climate of the last 10 million years, *Quat. Sci. Rev.*, *10*(4), 297–317.

Bierman, P., and E. J. Steig (1996), Estimating rates of denudation using cosmogenic isotope abundances in sediment, *Earth Surf. Processes Landforms*, *21*(2), 125–139.

Bishop, P. (1995), Drainage rearrangement by river capture, beheading and diversion, *Prog. Phys. Geogr.*, *19*(4), 449–473.

Blum, M. D., and T. E. Törnqvist (2000), Fluvial responses to climate and sea-level change: A review and look forward, *Sedimentology*, *47*, 2–48.

Bobst, A. L., T. K. Lowenstein, T. E. Jordan, L. V. Godfrey, T.-L. Ku, and S. Luo (2001), A 106 ka paleoclimate record from drill core of the Salar de Atacama, northern Chile, *Palaeogeogr. Palaeoclimatol. Palaeoecol.*, *173*, 21–42.

Boers, N., B. Bookhagen, N. Marwan, J. Kurths, and J. Marengo (2013), Complex networks identify spatial patterns of extreme rainfall events of the South American Monsoon System, *Geophys. Res. Lett.*, *40*, 1–7, doi:10.1002/grl.50681.

Boers, N., B. Bookhagen, N. Marwan, and J. Kurths (2015), Spatiotemporal characteristics and synchronization of extreme rainfall in South America with focus on the Andes Mountain range, *Clim. Dyn.*, doi:10.1007/s00382-015-2601-6, in press.

Bookhagen, B., and M. R. Strecker (2008), Orographic barriers, high-resolution TRMM rainfall, and relief variations along the eastern Andes, *Geophys. Res. Lett.*, *35*, L06403, doi:10.1029/2007GL032011.

Bookhagen, B., and M. R. Strecker (2012), Spatiotemporal trends in erosion rates across a pronounced rainfall gradient: Examples from the southern Central Andes, *Earth Planet. Sci. Lett.*, *327–328*, 97–110.

Bracken, L. J., L. Turnbull, J. Wainwright, and P. Bogaart (2015), Sediment connectivity: A framework for understanding sediment transfer at multiple scales, *Earth Surf. Processes Landforms*, *40*(2), 177–188.

Brown, E. T., R. F. Stallard, M. C. Larsen, D. L. Bourlès, G. M. Raisbeck, and F. Yiou (1998), Determination of predevelopment denudation rates of an agricultural watershed (Cayaguás River, Puerto Rico) using in-situ-produced ^{10}Be in river-borne quartz, *Earth Planet. Sci. Lett.*, *160*, 723–728.

Brown, E. T., R. F. Stallard, M. C. Larsen, G. M. Raisbeck, and F. Yiou (1995), Denudation rates determined from the accumulation of in situ-produced ^{10}Be in the Luquillo Experimental Forest, Puerto Rico, *Earth Planet. Sci. Lett.*, *129*, 193–202.
Bull, W. B. (1979), Threshold of critical power in streams, *Geol. Soc. Am. Bull.*, *90*, 453–464.
Bull, W. B. (1991), *Geomorphic Responses to Climate Change*, 326 pp., Oxford Univ. Press, London.
Carretier, S., et al. (2015), Differences in ^{10}Be concentrations between river sand, gravel and pebbles along the western side of the central Andes, *Quat. Geochronol.*, *27*, 33–51.
Castellanos, A. (1950), El Uquiense, Sedimentos Neógenos de Uquía (Senador Pérez) en la Provincia de Jujuy (Argentina), in *Facultad de Ciencias Matemáticas Físicas y Químicas y Naturales de la Universidad Nacional del Litoral*, *Serie Técnico Científico*, vol. 36, 55 pp., Rosario.
Cavalli, M., S. Trevisani, F. Comiti, and L. Marchi (2013), Geomorphic assessment of spatial sediment connectivity in small Alpine catchments, *Geomorphology*, *188*, 31–41.
Cruz, F. W., Jr., S. J. Burns, I. Karmann, W. D. Sharp, M. Vuille, A. O. Cardoso, J. A. Ferrari, P. L. Silva Dias, and O. Viana Jr. (2005), Insolation-driven changes in atmospheric circulation over the past 116,000 years in subtropical Brazil, *Nature*, *434*, 63–66.
Dadson, S. J., et al. (2004), Earthquake-triggered increase in sediment delivery from an active mountain belt, *Geology*, *32*(8), 733–736.
DiBiase, R. A., and K. X. Whipple (2012), The influence of erosion thresholds and runoff variability on the relationships among topography, climate, and erosion rate, *J. Geophys. Res.*, *116*, F04036, doi:10.1029/2011JF002095.
Donnelly, T. W. (1982), Worldwide continental denudation and climatic deterioration during the late Tertiary: Evidence from deep-sea sediments, *Geology*, *10*, 451–454.
Fontugne, M., R. Usselmann, D. Lavallée, M. Julien, and C. Hatté (1999), El Niño variability in the coastal desert of southern Peru during the mid-Holocene, *Quat. Res.*, *52*, 171–179.
Fritz, S. C., P. A. Baker, T. K. Lowenstein, G. O. Seltzer, C. A. Rigsby, G. S. Dwyer, P. M. Tapia, K. K. Arnold, K. Teh Lung, and S. Luo (2004), Hydrologic variation during the last 170,000 years in the Southern Hemisphere tropics of South America, *Quat. Res.*, *61*, 95–104.
Fryirs, K. A., G. J. Brierley, N. J. Preston, and M. Kasai (2007a), Buffers, barriers and blankets: The (dis)connectivity of catchment-scale sediment cascades, *Catena*, *70*(1), 49–67.
Fryirs, K. A., G. J. Brierley, N. J. Preston, and J. Spencer (2007b), Catchment-scale (dis)connectivity in sediment flux in the upper Hunter catchment, New South Wales, Australia, *Geomorphology*, *84*(3–4), 297–316.
Galbraith, R. F., R. G. Roberts, G. M. Laslett, H. Yoshida, and J. M. Olley (1999), Optical dating of single and multiple grains of quartz from Jinmium Rock Shelter, northern Australia: Part I, experimental design and statistical models, *Archaeometry*, *41*(2), 339–364.
Galliski, M., and J. G. Viramonte (1988), The Cretaceous paleorift in Northwestern Argentina: A petrologic approach, *J. S. Am. Earth Sci.*, *1*(4), 329–342.
Garreaud, R., M. Vuille, and A. C. Clement (2003), The climate of the Altiplano: Observed current conditions and mechanisms of past changes, *Palaeogeogr. Palaeoclimatol. Palaeoecol.*, *194*, 5–22.
Godfrey, L. V., T. E. Jordan, T. K. Lowenstein, and R. L. Alonso (2003), Stable isotope constraints on the transport of water to the Andes between 22° and 26°S during the last glacial cycle, *Palaeogeogr. Palaeoclimatol. Palaeoecol.*, *194*, 299–317.
Granger, D. E., J. W. Kirchner, and R. Finkel (1996), Spatially averaged long-term erosion rates measured from in situ-produced cosmogenic nuclides in alluvial sediment, *J. Geol.*, *104*(3), 249–257.
Hermanns, R. L., and M. R. Strecker (1999), Structural and lithological controls on large Quaternary rock avalanches (sturzstroms) in arid northwestern Argentina, *Geol. Soc. Am. Bull.*, *11*(6), 934–948.
Hermanns, R. L., S. Niedermann, S. Ivy-Ochs, and P. W. Kubik (2004), Rock avalanching into a landslide-dammed lake causing multiple dam failures in las Conchas valley (NW Argentina)—Evidence from surface exposure dating and stratigraphic analyses, *Landslides*, *1*, 113–122.
Hidy, A. J., J. C. Gosse, J. L. Pederson, J. P. Mattern, and R. C. Finkel (2010), A geologically constrained Monte Carlo approach to modeling exposure ages from profiles of cosmogenic nuclides: An example from Lees Ferry, Arizona, *Geochem. Geophys. Geosyst.*, *11*, Q0AA10, doi:10.1029/2010GC003084.
Horton, R. E. (1945), Erosional development of streams and their drainage basins: Hydrophysical approach to quantitative morphology, *Geol. Soc. Am. Bull.*, *56*, 275–370.
Hoth, S., J. Adam, N. Kukowski, and O. Oncken (2006), Influence of erosion on the kinematics of bivergent orogens: Results from scaled sandbox simulations, in *Tectonics, Climate, and Landscape Evolution*, *Geol. Soc. Am. Spec. Pap.*, vol. 398, edited by S. D. Willett et al., pp. 201–225.
Inman, D. L., and S. A. Jenkins (1999), Climate change and the episodicity of sediment flux of small California rivers, *J. Geol.*, *107*(3), 251–270.
Istanbulluoglu, E., and R. L. Bras (2006), On the dynamics of soil moisture, vegetation, and erosion: Implications of climate variability and change, *Water Resour. Res.*, *42*, W06418, doi:10.1029/2005WR004113.
Hovius, N., P. Meunier, C.-W. Lin, H. Chen, Y.-G. Chen, S. Dadson, M.-J. Horng, and M. Lines (2011), Prolonged seismically induced erosion and the mass balance of a large earthquake, *Earth Planet. Sci. Lett.*, *304*(3–4), 347–355.
Keefer, D. K., M. E. Moseley, and S. D. deFrance (2003), A 38,000-year record of floods and debris flows in the Ilo region of southern Peru and its relation to El Niño events and great earthquakes, *Palaeogeogr. Palaeoclimatol. Palaeoecol.*, *194*, 41–77.
Koons, P. O. (1990), Two-sided orogen: Collision and erosion from the sandbox to the Southern Alps, New Zealand, *Geology*, *18*(8), 679–682.
Knox, J. C. (1993), Large increases in flood magnitude in response to modest changes in climate, *Nature*, *361*, 430–432.
Kühn, F. (1923), *Algunos Rasgos Morfológicos de la Región Omaguaca*, *Anales de la Facultad de Ciencias de la Educación, Tomo I*, pp. 177–196, Universidad Nacional del Litoral, Santa Fe, Argentina.
Lague, D., N. Hovius, and P. Davy (2005), Discharge, discharge variability, and the bedrock channel profile, *J. Geophys. Res.*, *110*, F04006, doi:10.1029/2004JF000259.
Lal, D. (1991), Cosmic ray labeling of erosion surfaces: In situ nuclide production rates and erosion models, *Earth Planet. Sci. Lett.*, *104*(1–2), 424–439.
Magilligan, F. J., and P. S. Goldstein (2001), El Niño floods and culture change: A late Holocene flood history for the Río Moquegua, southern Peru, *Geology*, *29*, 431–434.
Magilligan, F. J., P. S. Goldstein, G. B. Fisher, B. C. Bostick, and R. B. Manners (2008), Late Quaternary hydroclimatology of a hyper-arid Andean watershed: Climate change, floods, and hydrologic responses to the El Niño-Southern Oscillation in the Atacama Desert, *Geomorphology*, *101*, 14–32.
Marc, O., N. Hovius, P. Meunier, T. Uchida, and S. Hayashi (2015), Transient changes of landslide rates after earthquakes, *Geology*, *43*, 883–886.
Margirier, A., L. Audin, J. Carcaillet, S. Schwartz, and C. Benavente (2015), Tectonic and climatic controls on the Chuquibamba landslide (Western Andes, southern Peru), *Earth Surf. Dyn.*, *3*, 281–289.
Marquillas, R. A., C. DelPapa, and I. F. Sabino (2005), Sedimentary aspects and paleoenvironmental evolution of a rift basin: Salta Group (Cretaceous-Paleogene), northwestern Argentina, *Int. J. Earth Sci. (Geol.Rundsch.)*, *94*(1), 94–113.

Marrett, R. A., R. W. Allmendinger, R. N. Alonso, and R. E. Drake (1994), Late Cenozoic tectonic evolution of the Puna Plateau and adjacent foreland, Northwestern Argentine Andes, *J. S. Am. Earth Sci.*, *7*(2), 179–207.
Marshall, L. G., R. F. Butler, R. E. Drake, and G. H. Curtis (1982), Geochronology of type uquian (late Cenozoic) land mammal age, *Argent. Sci.*, *216*(4549), 986–989.
Matmon, A., P. R. Bierman, J. Larsen, S. Southworth, M. Pavich, R. Finkel, and M. Caffee (2003), Erosion of an ancient mountain range, the Great Smoky Mountains, North Carolina and Tennessee, *Am. J. Sci.*, *303*(9), 817–855.
May, J., and R. D. Soler (2010), Late Quaternary morphodynamics in the Quebrada de Purmamarca, NW Argentina, *Quat. Sci. J.*, *59*(1–2), 21–35.
McFadden, L. D., S. G. Wells, and M. J. Jercinovich (1987), Influences of eolian and pedogenic processes on the origin and evolution of desert pavements, *Geology*, *15*, 504–508.
McGlue, M. M., A. S. Cohen, G. S. Ellis, and A. L. Kowler (2013), Late Quaternary stratigraphy, sedimentology and geochemistry of an underfilled lake basin in the Puna plateau (northwest Argentina), *Basin Res.*, *25*, 638–658.
McIntyre, A., W. F. Ruddiman, K. Karlin, and A. C. Mix (1989), Surface water response of the equatorial Atlantic Ocean to orbital forcing, *Paleoceanography*, *4*(1), 19–55, doi:10.1029/PA004i001p00019.
McPhillips, D., P. R. Bierman, and D. H. Rood (2014), Millenial-scale record of landslides in the Andes consistent with earthquake trigger, *Nat. Geosci.*, *7*, 925–930.
Meade, R. H. (1982), Sources, sinks, and storage of river sediment in the Atlantic drainage of the United States, *J. Geol.*, *90*(3), 235–252.
Miller, D. J., and L. E. Benda (2000), Effects of punctuated sediment supply on valley-floor landforms and sediment transport, *Geol. Soc. Am. Bull.*, *112*(12), 1814–1824.
Molfino, B., and A. McIntyre (1990), Precessional forcing of nutricline dynamics in the Equatorial Atlantic, *Science*, *249*(4970), 766–769.
Molnar, P. (2001), Climate change, flooding in arid environments, and erosion rates, *Geology*, *29*(12), 1071–1074.
Molnar, P. (2004), Late Cenozoic increase in accumulation rates of terrestrial sediment: How might climate change have affected erosion rates?, *Annu. Rev. Earth Planet. Sci.*, *32*, 67–89.
Molnar, P., R. S. Anderson, G. Kier, and J. Rose (2006), Relationships among probability distributions of stream discharges in floods, climate, bed load transport, and river incision, *J. Geophys. Res.*, *111*, F02001, doi:10.1029/2005JF000310.
Montgomery, D. R., and W. E. Dietrich (1992), Channel initiation and the problem of landscape scale, *Science*, *255*, 826–830.
Moya, M. C. (1988), Lower Ordovician in the southern part of the argentine Eastern Cordillera, in *The Southern Central Andes*, *Frontiers in Earth Sciences*, vol. 17, edited by H. Bahlburg et al., pp. 55–69, Springer, Berlin.
Murray, A. S., and J. M. Olley (2002), Precision and accuracy in the optically stimulated luminescence dating of sedimentary quartz, *Geochronometria*, *21*, 16.
Nester, P. L., E. Gayó, C. Latorre, T. E. Jordan, and N. Blanco (2007), Perennial stream discharge in the hyperarid Atacama Desert of northern Chile during the latest Pleistocene, *Proc. Nat. Acad. Sci.*, *104*(50), 19,724–19,729.
Niemi, N. A., M. Oskin, D. W. Burbank, A. J. Heimsath, and E. J. Gabet (2005), Effects of bedrock landslides on cosmogenically determined erosion rates, *Earth Planet. Sci. Lett.*, *237*, 480–498.
Olen, S., B. Bookhagen, B. Hoffmann, D. Sachse, D. Adhikari, and M. R. Strecker (2015), Understanding erosion rates in the Himalaya: A case study from the Arun Valley, *J. Geophys. Res. Earth Surf.*, *120*, 2080–2102, doi:10.1029/2014JF003410.
Omarini, R. (1983), Caracterización Litológica, Diferenciación y Génesis de la Formación Puncoviscana Entre el Valle de Lerma y la Faja Eruptiva de la Puna, Unpublished thesis, Universidad Nacional de Salta, Argentina.
Ouchi, S. (1985), Response of alluvial rivers to slow active tectonic movement, *Geol. Soc. Am. Bull.*, *96*, 504–515.
Paolini, L., R. Villalba, and H. R. Grau (2005), Precipitation variability and landslide occurrence in a subtropical mountain ecosystem of NW Argentina, *Dendrochronologia*, *22*(3), 175–180.
Pingel, H., R. N. Alonso, A. Mulch, A. Rohrmann, M. Sudo, and M. R. Strecker (2014), Pliocene orographic barrier uplift in the southern Central Andes, *Geology*, *42*(8), 691–694.
Pingel, H., M. R. Strecker, R. N. Alonso, and A. K. Schmitt (2013), Neotectonic basin and landscape evolution in the Eastern Cordillera of NW Argentina, Humahuaca Basin (~24°S), *Basin Res.*, *25*, 554–573.
Placzek, C., J. Quade, and P. J. Patchett (2006), Geochronology and stratigraphy of late Pleistocene lake cycles on the southern Bolivian Altiplano: Implications for causes of tropical climate change, *Geol. Soc. Am. Bull.*, *118*(5–6), 515–532.
Prescott, J. R., and J. T. Hutton (1994), Cosmic ray contributions to dose-rates for luminescence and ESR dating: Large depths and long-term time variations, *Radiat. Meas.*, *23*(2/3), 497–500.
Puchol, N., J. Lavé, M. Lupker, P.-H. Blard, F. Gallo, and C. France-Lanord (2014), Grain-size dependent concentration of cosmogenic ^{10}Be and erosion dynamics in a landslide-dominated Himalayan watershed, *Geomorphology*, *224*, 55–68.
Quade, J., J. A. Rech, J. L. Betancourt, C. Latorre, B. Quade, K. A. Rylander, and T. Fisher (2008), Paleowetlands and regional climate change in the central Atacama Desert, northern Chile, *Quat. Res.*, *69*, 343–360.
Rhodes, E. J. (2011), Optically stimulated luminescence dating of sediments over the past 200,000 years, *Ann. Rev. Earth Planet. Sci.*, *39*, 461–488.
Rittenour, T. M. (2008), Luminescence dating of fluvial deposits: Applications to geomorphic, palaeoseismic and archaeological research, *Boreas*, *37*(4), 613–635.
Robinson, R. A. J., J. Q. G. Spencer, M. R. Strecker, A. Richter, and R. N. Alonso (2005), Luminescence dating of alluvial fans in intramontane basins of NW Argentina, in *Alluvial Fans: Geomorphology, Sedimentology, Dynamics Harvey*, *Geol. Soc. London, Spec. Publ.*, vol. 251, edited by A. M. Mather et al., pp. 153–168, London.
Salfity, J. A. (1982), Evolución paleogeográfica del Grupo Salta (Cretácico-Eogénico), Argentina, *Actas V Congr. Latinoamerican Geol.*, *1*, 11–26.
Salfity, J. A., E. M. Brandán, C. R. Monaldi, and E. F. Gallardo (1984), Tectónica compresiva Cuaternaria en la Cordillera Oriental Argentina latitud de Tilcara (Jujuy), *Actas IX Congr. Geol. Argent.*, *2*, 427–434.
Sánchez, M., and J. A. Salfity (1999), La cuenca Cámbrica del Grupo Mesón en el Noroeste Argentino: Desarrollo estratigráfico y paleogeográfico, *Actas Geol. Hispánica*, *34*(2–3), 123–139.
Sancho, C., J. L. Peña, F. Rivelli, E. Rhodes, and A. Muñoz (2008), Geomorphological evolution of the Tilcara alluvial fan (Jujuy Province, NW Argentina): Tectonic implications and palaeoenvironmental considerations, *J. South Am. Earth Sci.*, *26*(1), 68–77.
Savi, S., M. Schneuwly-Bollschweiler, B. Bommer-Denns, M. Stoffel, and F. Schlunegger (2013), Geomorphic coupling between hillslopes and channels in the Swiss Alps, *Earth Surf. Processes Landforms*, *38*, 959–969.
Savi, S., K. Norton, V. Picotti, F. Brardinoni, N. Akçar, P. W. Kubik, R. Delunel, and F. Schlunegger (2014), Effects of sediment mixing on ^{10}Be concentrations in the Zielbach catchment, central-eastern Italian Alps, *Quat. Geochronol.*, *19*, 148–162.
Scherler, D., B. Bookhagen, and M. R. Strecker (2014a), Tectonic control on ^{10}Be-derived erosion rates in the Garhwal Himalaya, India, *J. Geophys. Res. Earth Surf.*, *119*, 83–105, doi:10.1002/2013JF002955.

Scherler, D., H. Munack, J. Mey, P. Eugster, H. Wittmann, A. T. Codilean, P. Kubik, and M. R. Strecker (2014b), Ice dams, outburst floods, and glacial incision at the western margin of the Tibetan Plateau: A >100-kyr chronology from the Shyok Valley, Karakoram, *Geol. Soc. Am. Bull.*, *126*(5-6), 738–758.

Scherler, D., B. Bookhagen, H. Wulf, F. Preusser, and M. R. Strecker (2015), Increased late Pleistocene erosion rates during fluvial aggradation in the Garhwal Himalaya, northern India, *Earth Planet. Sci. Lett.*, *428*, 255–266.

Schneider, R. R., P. J. Müller, and G. Ruhland (1995), Late Quaternary surface circulation in the east equatorial South Atlantic: Evidence from Alkenone sea surface temperatures, *Palaeoceanography*, *10*(2), 197–219.

Schwanghart, W., and D. Scherler (2014), TopoToolbox 2—MATLAB-based software for topographic analysis and modeling in Earth surface sciences, *Earth Surf. Dyn.*, *2*, 1–7.

Spencer, J. Q. G., and R. A. J. Robinson (2008), Dating intramontane alluvial deposits from NW Argentina using luminescence techniques: Problems and potential, *Geomorphology*, *93*, 144–155.

Spencer, J. Q., D. C. W. Sanderson, K. Deckers, and A. A. Sommerville (2003), Assessing mixed dose distributions in young sediments identified using small aliquots and a simple two-step SAR procedure: The F-statistic as a diagnostic tool, *Radiat. Meas.*, *37*, 425–431.

Steffen, D., F. Schlunegger, and F. Preusser (2009), Drainage basin response to climate change in the Pisco valley, Peru, *Geology*, *37*(6), 491–494.

Steffen, D., F. Schlunegger, and F. Preusser (2010), Late Pleistocene fans and terraces in the Majes valley, southern Peru, and their relation to climatic variations, *Int. J. Earth Sci.*, *99*, 1975–1989.

Stone, J. O. (2000), Air pressure and cosmogenic isotope production, *J. Geophys. Res.*, *105*(B10), 23,753–23,759, doi:10.1029/2000JB900181.

Strecker, M. R., R. N. Alonso, B. Bookhagen, B. Carrapa, G. E. Hilley, E. R. Sobel, and M. H. Trauth (2007), Tectonics and climate of the Southern Central Andes, *Ann. Rev. Earth Planet. Sci.*, *35*, 747–787.

Strecker, M. R., R. Alonso, B. Bookhagen, B. Carrapa, I. Coutand, M. P. Hain, G. E. Hilley, E. Mortimer, L. Schoenbohm, and E. R. Sobel (2009), Does the topographic distribution of the central Andean Puna Plateau result from climatic or geodynamic processes?, *Geology*, *37*(7), 643–646.

Streit, R. L., D. W. Burbank, M. R. Strecker, R. N. Alonso, J. M. Cottle, and A. R. C. Kylander-Clark (2015), Controls on intermontane basin filling, isolation and incision on the margin of the Puna Plateau, NW Argentina (~23°S), *Basin Res.*, doi:10.1111/bre.12141, in press.

Summerfield, M. A. (1991), *Global Geomorphology: An Introduction to the Study of Landforms*, 537 pp., Longman/Wiley, London/New York.

Tchilinguirian, P., and F. X. Pereyra (2001), Geomorfología del sector Salinas Grandes—Quebrada de Humahuaca, provincial de Jujuy, *Rev. Asoc. Geol. Argent.*, *56*(1), 3–15.

Thomsen, K. J., A. S. Murray, L. Botter-Jensen, and J. Kinahan (2007), Determination of burial dose in incompletely bleached fluvial samples using single grains of quartz, *Radiat. Meas.*, *42*(3), 370–379.

Trauth, M. H., R. A. Alonso, K. R. Haselton, R. L. Hermanns, and M. R. Strecker (2000), Climate change and mass movements in the NW Argentine Andes, *Earth Planet. Sci. Lett.*, *179*, 243–256.

Trauth, M. H., B. Bookhagen, N. Marwan, and M. R. Strecker (2003), Multiple landslide clusters record Quaternary climate changes in the northwestern Argentine Andes, *Palaeogeogr. Palaeoclimatol. Palaeoecol.*, *194*, 109–121.

Trenberth, K. E. (2011), Changes in precipitation with climate change, *Clim. Res.*, *47*(1), 123–138.

Tucker, G. E. (2004), Drainage basin sensitivity to tectonic and climatic forcing: Implications of a stochastic model for the role of entrainment and erosion thresholds, *Earth Surf. Processes Landforms*, *29*(2), 185–205.

Tucker, G. E., and R. L. Bras (2000), A stochastic approach to modeling the role of rainfall variability in drainage basin evolution, *Water Resour. Res.*, *36*(7), 1953–1964, doi:10.1029/2000WR900065.

Tucker, G. E., and R. Slingerland (1997), Drainage basin response to climate change, *Water Resour. Res.*, *33*, 2031–2047, doi:10.1029/97WR00409.

Turner, J. C. M. (1960), Estratigrafía de la Sierra de Santa Victoria y adyacencias, *Bol. Acad. Nac. Ciencias Córdoba*, *41*(2), 163–196.

Vera, C., et al. (2006), Toward a unified view of the American monsoon systems, *J. Clim.*, *19*(20), 4977–5000.

von Blanckenburg, F. (2005), The control mechanisms of erosion and weathering at basin scale from cosmogenic nuclides in river sediment, *Earth Planet. Sci. Lett.*, *237*(3–4), 462–479.

Wallinga, J., A. S. Murray, and L. Botter-Jensen (2002), Measurement of the dose in quartz in the presence of feldspar contamination, *Radiat. Prot. Dosim.*, *101*(1–4), 367–370.

Walther, A., M. Orgeira, M. Reguero, D. Verzi, J. Vilas, R. N. Alonso, E. Gallado, S. Kelly, and T. E. Jordan (1998), Estudio Paleomagnético, Paleontológico y Radimétrico de la Formación Uquía (Plio-Pleistoceno) en Esquina Blanca (Jujuy), *Actas X Congr. Latinoamericano Geol. y VI Congr. Nacional Geol. Económ.*, *1*, 77, Buenos Aires, Argentina.

Wang, X., A. S. Auler, R. L. Edwards, H. Cheng, E. Ito, Y. Wang, X. Kong, and M. Solheid (2007), Millennial-scale precipitation changes in southern Brazil over the past 90,000 years, *Geophys. Res. Lett.*, *34*, L23701, doi:10.1029/2007GL031149.

Wayne, W. J. (1999), The Alemanía rockfall dam: A record of a mid-Holocene earthquake and catastrophic flood in northwestern Argentina, *Geomorphology*, *27*(3–4), 295–306.

Whipple, K. X., and B. J. Meade (2006), Orogen response to changes in climatic and tectonic forcing, *Earth Planet. Sci. Lett.*, *243*(1–2), 218–228.

Willett, S. (1999), Orogeny and orography: The effects of erosion on the structure of mountain belts, *J. Geophys. Res.*, *104*(B12), 28,957–28,981, doi:10.1029/1999JB900248.

Yanites, B. J., G. E. Tucker, and R. S. Anderson (2009), Numerical and analytical models of cosmogenic radionuclide dynamics in landslide-dominated drainage basins, *J. Geophys. Res.*, *114*, F01007, doi:10.1029/2008JF001088.

York, D., N. M. Evensen, M. L. Martínez, and J. D. B. Delgado (2004), Unified equations for slope, intercept, and standard errors of the best straight line, *Am. J. Phys.*, *72*(3), 367–375.

Zhang, P., P. Molnar, and W. R. Downs (2001), Increased sedimentation rates and grain sizes 2–4 Myr ago due to the influence of climate change on erosion rates, *Nature*, *410*, 891–897.